Am Min 5287 Revision 1

Polycrystallinity of green rust minerals and their synthetic analogs: Implications for particle formation and reactivity in complex systems

Carol A. Johnson,[1*] Mitsuhiro Murayama,[2] Kirsten Küsel,[3,4] and Michael F. Hochella Jr.[1]

[1]Department of Geosciences, Virginia Tech, Blacksburg, VA 24061, USA

[2]Department of Materials Science and Engineering, Virginia Tech, Blacksburg, VA 24061, USA

[3]Institute of Ecology, Friedrich Schiller University Jena, D-07743 Jena, Germany

[4]German Centre for Integrative Biodiversity Research (iDiv) Halle-Jena-Leipzig, D-04103 Leipzig, Germany

[*]Corresponding author: caroljohnson49@gmail.com

Present address: C.A. Johnson now at Department of Civil and Environmental Engineering, Duke University, Durham, NC 27708-0287, USA

ABSTRACT

We demonstrate in this study that natural green rust nanoparticles and their synthetic analogs can be complex polycrystalline phases composed of crystallites only a few nanometers in size, and often include nanometer-sized regions of amorphous material. The natural green rusts are Zn-bearing pseudo-hexagonal platelets previously identified by us in the contaminated mine drainage of the former Ronneburg uranium mine in Germany (Johnson et al. 2014). We also identified Ni- and Cu-bearing green rust platelets in the sediment underlying the drainage outflow 20 m downstream, and, using dark field transmission electron microscopy (DF-TEM),

found that these natural green rusts are not usually structurally-coherent single crystals. Synthetic sulfate green rusts are also polycrystalline and composed of crystallites of only a few nanometers in size, though different synthesis conditions produced different patterns of polycrystallinity. While pseudo-hexagonal platelets are the typical morphology of green rust, we also synthesized green rust nanorods, which have not previously been reported. In addition to the known characteristics of green rusts (including a very large aspect ratio and surface area to volume ratio, and the redox properties allowed by the structural mixture of Fe^{II} and Fe^{III}), these polycrystalline platelets exhibit a high abundance of defect sites and likely a rough surface topography. The combination of these characteristics has important implications for the reactivity of green rust with biogeochemical interfaces in natural and anthropogenic systems.

KEYWORDS: Nanorod, nanoparticle, layered-double-hydroxide, iron oxide, transmission electron microscopy, texture, oriented aggregation, mine drainage

INTRODUCTION

There are many factors that influence mineral interactions with the surrounding components of Earth systems. Composition, surface atomic structure, crystal morphology, size, surface charge and surface topography are just a few mineral properties that affect their behavior in these complex natural settings (Hochella Jr et al. 2012 and references therein). Nanoparticles have especially high reactivity compared to larger particles due to their small size (high surface area to volume ratio) and comparatively high-energy surface topography and atomic structure. Nanoparticles of the extensive family of iron oxides and their roles in the overall biogeochemical cycling of iron on Earth have been comprehensively studied, as well as the intimate link with the

fate and transport of environmental pollutants (e.g. Banfield and Zhang 2001; Waychunas et al. 2005; Raiswell 2011; Taylor and Konhauser 2011; Dong and Lu 2012; and many references therein). However, geochemists continue to discover nanoscale nuances about iron oxide mineral structure and composition that change the way we think about their interactions with environmental systems. For example, schwertmannite is an iron oxyhydroxysulfate phase that is considered to be a mineral, but upon careful examination by high resolution transmission electron microscopy (HR-TEM), natural samples were found to consist of both nanocrystalline and amorphous domains (French et al. 2012). The long-range order that is fundamental to the definition of a mineral does not exist in these natural samples. Studies like these that use analytical TEM techniques are useful for determining heterogeneities in nanoscale composition and structure, which highly influence a mineral's reactivity with its surroundings. Minerals with shorter range order, abundant structural defects, and variable/gradational compositions are likely quite common in nature (Caraballo et al. 2015, and references therein).

In the complex system of anoxic underground mine drainage, another example of an iron oxide mineral, green rust, was found that appears to contain both areas of crystalline and amorphous material (Johnson et al. 2014), which warranted further investigation. Green rusts are a family of minerals that contain both reduced and oxidized iron species (Fe^{II} and Fe^{III}) within iron hydroxide layers (aka a layered double hydroxide, or LDH), separated by an interlayer containing a wide array of anions and cations somewhat analogous to clays (Trolard and Bourrié 2012). They typically are found as very thin pseudo-hexagonal platelets, from a few to a few tens of nanometers thick (Christiansen et al. 2009; Trolard and Bourrié 2012; Johnson et al. 2014). Keeping in mind that the crystal repeat distance in the plate thickness direction is close to one nanometer, these plates that are typically hundreds to thousands of nanometers wide can have a

high surface to volume ratio. This, combined with the mixed valence states of iron present (plus other crystal structural elements discovered in this study and discussed in detail below), results in a high potential for chemical reaction.

In nature, green rusts have been found to take up Ni (Zegeye et al. 2012) and Zn (Johnson et al. 2014). Synthesized green rusts have been shown to reduce a variety of metals (coupled to structural Fe^{II} oxidation) such as Cr^{VI} (Williams and Scherer 2001; Skovbjerg et al. 2006) and Ag^{I}, Ag^{III}, Cu^{II}, and Hg^{II} (O'Loughlin et al. 2003), to reduce or dechlorinate organics such as CCl_4 (Erbs et al. 1999) and dichloroethylene (Han et al. 2012), and to sorb As (Jönsson and Sherman 2008) and Ni (Parmar and Beveridge 2001). Green rusts are also commonly found as a corrosion product of steels (Stampfl 1969; Swietlik et al. 2012).

Research on the structure and reactivity of the green rust family has increased considerably in the past decade. Nevertheless, compared to other iron oxide minerals such as goethite, hematite, or even poorly crystalline ferrihydrite and schwertmannite, large gaps in a thorough understanding of green rusts remain. Green rust was only first positively identified in nature in 1997, in a reductomorphic soil (Trolard et al. 1997), and since then has only been conclusively identified in relatively few natural sites for example in groundwater (Christiansen et al. 2009), mine drainage sediments (Bearcock et al. 2006), an iron-rich lake (Zegeye et al. 2012), and a mofette soil (Rennert et al. 2012). It can form biotically from the bacterial reduction of various iron oxides such as lepidocrocite (Ona-Nguema et al. 2002; O'Loughlin et al. 2007; Jorand et al. 2013), ferrihydrite (Kukkadapu et al. 2004), and hydrous ferric oxide (Parmar and Beveridge 2001). Green rust can also form abiotically for example via the oxidation of $Fe(OH)_2(s)$ (Génin et al. 2006) and the interaction of dissolved Fe^{II} with ferric oxides (Géhin et al. 2002; Ruby et al. 2003; Usman et al. 2012).

A specific type of green rust, fougerite, was only accepted as the first green rust mineral in 2004 (Trolard et al. 2007), but the structures and formulas for different green rusts are continuously re-evaluated and modified (Mills et al. 2012). For example, Simon et al. (2003) determined sulfate green rust (GR-SO_4, $Fe^{II}_4Fe^{III}_2(OH)_{12}$ SO_4•~$8H_2O$) to be in the *P*-31*m* {note to typesetters: all minus signs in the space groups are overbars} space group (#162) with lattice parameters of $a = b = 5.524$ Å, c = 11.011 Å, and an interlayer arrangement characteristic of the hydrotalcite group (within the hydrotalcite supergroup). Then Christiansen et al. (2009) further refined the formula for sulfate green rust to be $NaFe^{II}_6Fe^{III}_3(SO_4)_2(OH)_{18}$•$12H_2O$ (now designated GR-Na,SO_4), thereby rearranging the SO_4^{2-} molecules in the interlayer and showing how Na^+ is necessary for charge balance. The crystallographic space group for GR-Na,SO_4 is *P*-3 (#147) with $a = b = 9.529$ Å, $c = 10.969$ Å and an interlayer arrangement characteristic of the nikischerite group (still within the hydrotalcite supergroup) (Christiansen et al. 2009).

Green rust minerals are generally thought to be geochemically important and widespread in anoxic settings. We suspect that it is only rarely collected in the field and preserved for analysis because it is exceptionally ephemeral under oxidizing conditions. In addition, while studies on synthetic green rusts have been performed in order to try to better understand their formation and reactivity, it is important to establish that the synthetic particles are reasonably similar to ones that are found in nature. Structure and composition are two critical mineral attributes that can be probed at the nanoscale with analytical TEM, making this a logical starting point for the comparison between natural and synthetic green rusts. The only published studies that include HR-TEM of green rusts indicate that they were single, coherent crystals (Skovbjerg et al. 2006; Zegeye et al. 2012), but our previous work has shown the possibility of less coherent nano-sized domains in the green rust from mine drainage outflow (Johnson et al. 2014). In this

study, we examined more thoroughly the same green rust particles from this mine outflow, as well as additional green rusts from sediments at the site, using dark field (DF) TEM. DF-TEM can be used to understand the structural coherency of the particles. It provides information about whether a particle is a single continuous crystal or polycrystalline. Polycrystalline materials will exhibit light and dark areas in the DF image, and fast Fourier transform (FFT) patterns calculated from HR-TEM images (equivalent to electron diffraction patterns) will show crystallite rotation and tilting. These same techniques, along with compositional analysis (nanoscale energy dispersive x-ray spectroscopy, EDS) were applied to sulfate green rusts that we synthesized in the laboratory to see if they exhibited similar features. With this information, we infer possible formation mechanisms and potential effect on reactivity.

MATERIALS AND METHODS

Natural green rust sampling and site characterization

Green rust mineral nanoparticles were identified in the anoxic outflow from the former Ronneburg uranium mine as previously reported in Johnson et al. (2014). Green rust particles were also identified in the sediment of iron-rich terraces at the same site, where the drainage water flows over a creek bank 20 m from the site of outflow. Sampling details, including the geochemical characteristics of water and sediment along the flow path, can be found in Johnson et al. (2014). Critical details are described here in brief. Water samples at the outflow site were collected by filling 50-mL plastic centrifuge tubes to the top, without headspace in order to reduce exposure to air. Sediment samples from the terrace site were also collected in a similar manner. Samples were handled thereafter in an anoxic chamber (Coy, 100% N_2 gas), and sediments were additionally diluted with deoxygenated ultrapure water (18.2 MΩ, flushed with

N_2, Milli-Q Advance, Millipore). The pH of the outflow water on October 25, 2011 (the date green rust was found) was 5.75, with a redox potential Eh of 260 mV (corrected to the standard hydrogen electrode) and a dissolved oxygen concentration of 0.6 mg/L. Concentrations of "dissolved" Fe^{II} (5.6(1) mM) and "dissolved" SO_4^{2-} (40(9) mM) were analyzed after water samples were filtered through a 0.2 μm filter and acidified in the field. In addition, the microbial community structure has been characterized and a number of iron oxidizing bacteria (related to *Gallionella spp.*, 49% of the community) and iron reducing bacteria (related to *Albidoferax ferrireducens* and *Geobacter spp*, 21%) were found in the outflow water on October 25, 2011 (Fabisch et al., submitted).

Green rust synthesis

Sulfate green rust (GR-A, -B, -C, -D) was synthesized via a co-precipitation synthesis method based on the methods from Géhin et al. (2002) and Ruby et al. (2003, 2006). A solution of NaOH (in a plastic bottle) was added by titrating slowly with a peristaltic pump or pouring rapidly into a solution of hydrated Fe^{II} and Fe^{III} sulfate salts ($FeSO_4 \bullet 7H_2O$, JT Baker, ACS reagent, freshly purchased and stored at 4°C; $Fe_2(SO_4)_3 \bullet nH_2O$, reagent brand and grade given in Table 1, with approximately six waters of hydration as determined by inductively coupled plasma atomic emission spectroscopy (ICP-AES, Arcos SOP, Spectro Analytical Instruments Inc)) while stirring vigorously with a stir bar. The syntheses were performed both in air with ultrapure water (Barnstead Nanopure, 18.2 MΩ) and in an anoxic chamber (Coy, N_2 gas with 1% H_2) with deoxygenated ultrapure water (boiled and purged with N_2 in a borosilicate glass bottle) in order to determine if the green rust structure was comparable when formed in oxic and anoxic conditions. Si contamination from boiling water in glass was an issue, and both plastic and glass

reaction vessels were ruled out as sources (see the discussion section). The key reaction parameters were the molar ratios nFe^{II}/nFe^{III} and nOH^-/nFe_{total}, which were varied, and given in Table 1 along with the general reaction conditions. In syntheses GR-A, -B, and -C, nFe^{II}/nFe^{III} was higher than the stoichiometric amount for GR-SO_4 ($nFe^{II}/nFe^{III} = 2$), while in GR-D it was lower. Green rust was produced in other syntheses but we report here only those that formed hexagonal particles (with the exception of GR-D) and that gave unique results from TEM analysis.

Transmission electron microscopy

Aliquots from both natural and synthetic samples were diluted with anoxic ultrapure water. A 10-µL drop was placed on a TEM grid (lacey carbon on copper or gold mesh, Electron Microscopy Sciences, or ultrathin carbon on lacey carbon on copper mesh, Ted Pella), and was immediately wicked away with a lint-free wipe, followed by rinsing twice with ultrapure deoxygenated water to remove salts while preventing oxidation. Sample grids were stored anoxically in a N_2-flushed plastic container (SampleSaver, South Bay Technologies). Scanning electron microscopy (SEM, FEI Quanta 600 and LEO Zeiss 1550 with field emission sources) was first used to scan some grids for areas of interest, followed by further analysis by TEM (primarily JEOL 2100 with a LaB_6 thermionic source operated at 200kV, also FEI Titan with a field emission source operated at 300kV). To mitigate beam damage, we reduced the beam current by over 80% using a 50 µm C2 aperture (compared to a 120 µm one) and a medium spot size. Structural information was obtained by both selected area electron diffraction (SAED) of large areas and fast Fourier transformation (FFT) of high-resolution images (HR-TEM) and analyzed using the program *Digital Micrograph* (Gatan Inc). Dark field (DF) imaging was used

to obtain information on the polycrystalline nature of the particles by placing a small (5 μm) objective aperture around the center beam and tilting the beam until the hkl reflection of interest (in SAED mode) was aligned with the aperture. In imaging mode, all areas of the crystal that diffract the electrons to that particular hkl appear bright. Particles that are single crystals will appear as one bright area, while polycrystalline particles will exhibit a spotty bright pattern with dark areas in-between. Elemental composition was obtained by energy dispersive X-ray spectroscopy (EDS), and semi-quantitative atomic percentages were calculated with the ratio (thin film approximation) standardless method using the program *Analysis Station* (JEOL Ltd). Nanoprobe EDS was performed on the FEI Titan operated in scanning transmission electron microscopy (STEM) mode, and Si/Fe atomic ratios were calculated using the program *TEM Imaging and Analysis* (TIA, FEI).

X-ray diffractometry

Sample aliquots were filtered through a 0.45-μm membrane and rinsed with a 1:1 solution of glycerol to deoxygenated ultrapure water, which allowed the material to be stable in air for at least 24 hours (as determined by comparing the XRD patterns at the beginning and end of this period). Material was scraped off the filters, lightly smeared onto a zero background silica plate or flat aluminum plate and analyzed (MiniFlexII, Rigaku, Cu Kα source, 30 kV, 15 mA, 0.02-0.5 °/step, 2 s/step, sample rotation). Some preferential orientation along the basal (001) plane occurred with this technique. An estimation of crystallite size based on peak broadening was calculated using the Scherrer equation, $L_{hkl} = \frac{\kappa\lambda}{\beta_{hkl}\cos\theta}$, where L is the crystallite size perpendicular to the hkl crystallographic plane, λ = the X-ray wavelength, β = is the full width at half maximum of the XRD peak in radians, and θ is the Bragg diffraction angle (Scherrer 1918;

Lavina et al. 2014). *K* is the Scherrer constant, or shape factor, which varies around unity (e.g. 0.89 for a spherical crystallite with no lattice strain (Klug and Alexander 1974), 0.94 for a cube (Klug and Alexander 1974), and 0.998 for a right cylinder (Vargas et al. 1983)). Crystallite sizes are over-estimated by this calculation due to a variety of factors that can cause peak broadening, including instrument factors and crystallite strain in addition to crystallite size and shape (Klug and Alexander 1974; Lavina et al. 2014). The Scherrer equation is only valid for crystallites less than about 100 nm (Lavina et al. 2014).

Potential sample artifacts

Despite the precautions we took to minimize exposure to air, some iron oxidation is inevitable due to the reactive nature of green rust. Containers of water samples containing natural green rust were filled to the top but a small air bubble was present. Samples were exposed to air for a few minutes at a time when the anoxic canister was opened during grid transfer into and out of the TEM. Unfortunately, the lack of rigorous TEM data from other studies makes it difficult to determine if this short-term, but repeated exposure to air affects sample structure. There are only two HR-TEM images of green rust in the literature available for comparison. The one most similar to the results of our work shows an image with both slightly disordered and very nearly amorphous regions of the synthetic green rust crystal, the origins of which were not discussed (Skovbjerg et al. 2006, Figure 8). The other shows a coherent single crystal without amorphous patches though that sample was reportedly only exposed to air for seconds (Zegeye et al. 2012, Figure 2f).

As described below in the results section, the green rust samples (i.e. GR-A and GR-B) had different patterns of polycrystallinity, unlike what might be expected if oxidation affected

the samples in a homogenous way. Although we still believe the underlying polycrystallinity of these green rusts is real, we cannot rule out polycrystallinity and amorphous areas as artifacts caused by oxidation. As described in the results section, the SAED patterns resulted in d-spacings that matched hematite. However, because we also have XRD evidence of green rust formation, we are confident that these particles once were green rust. In addition, the nanorods did not obviously exhibit oxidation artifacts though we expect they would be much more reactive than micron-sized platelets. Another possible source of nanoscale restructuring is the electron beam, but we only observed crystallization over time as opposed to areas becoming amorphous, and we minimized these by lowering the beam current (dose). Regardless of the presence of artifacts in this work, we still believe these results are useful and hopefully will spur more studies on preventing artifacts of reactive nanominerals.

RESULTS

Natural green rust

Pseudo-hexagonal green rust platelets up to approximately 1 μm in diameter (Figure 1) were found in microoxic, slightly acidic mine groundwater outflow site in samples taken from the former Ronneburg uranium mine (Germany) as was previously described in Johnson et al. (2014). Many other platelets were smaller and exhibited rounder edges, possibly in various stages of dissolution (see Figure 6a in Johnson et al. 2014), but had the exact same electron diffraction pattern as the pseudo-hexagonal platelets. Thus, we believe they have very similar crystal structures. In this study, we characterized them further by TEM.

The hexagonal electron diffraction pattern (e.g. Figure 2c) exhibited by the natural particles is not unique to green rust. The d-spacing values (2.56(7) and 1.50(3) Å) actually match

254 those for hematite oriented along the [001] zone axis (c-axis) (2.52 and 1.45 Å for hematite,
255 compared to 2.76 and 1.59 Å for sulfate green rust, see Table 2), but they also exactly match the
256 pattern and d-spacings for the synthetic materials in this study, which were verified to be sulfate
257 green rust by XRD (discussed below in Figure 4). The hkl reflection indices are identical for
258 hematite and sulfate green rust oriented along the [001], and we will therefore refer to indices
259 instead of d-spacings when discussing SAED and DF imaging. Throughout the remainder of this
260 paper, we have chosen the sulfate green rust II structure (*P*-31*m*) {note to typesetter: minus sign
261 is overbar} proposed by Simon et al. (2003) as our reference structure.
262 HR-TEM of the platelets as previously reported (Johnson et al. 2014) indicated the
263 possibility of a non-coherent green rust crystal structure, due to the presence of both amorphous
264 areas and nano-sized crystallites that were perhaps slightly misaligned. In this study, STEM EDS
265 with a spot size of approximately 1 nm was used to compare the compositions of the dark,
266 crystalline, regions that display lattice fringes, and light, amorphous, regions of the same particle,
267 which did not show lattice fringes (Figure 1). Dark regions had lower Si/Fe ratios (e.g. 0.12, 0.19
268 in two measurements made) compared to the light regions (e.g. 0.44, 0.47). Interestingly, Zn and
269 S were associated with the dark regions but not the light regions.
270 These results led to further investigations with a combination of HR-TEM and DF
271 imaging, as shown in Figure 2. The platelet shown in Figure 2a,b has a pseudo-hexagonal
272 morphology, and its SAED pattern (Figure 2c) shows a hexagonal arrangement with slightly
273 elongated spots that is typical of these platelets. Based on the assumed crystal structure, the
274 pattern was indexed to be a [001] zone axis pattern. Three DF images of the platelet (Figure 2d-f,
275 same area as in Figure 2b) were taken by selecting the 030,-330, and -300 {note to typesetter:
276 minus signs are overbars} reflections (circled in Figure 2c) in order to examine the coherence of

the platelet crystallinity. The crystallites contributing to the chosen reflection are represented in the image by bright areas, which in this case are only a few nm in diameter (2(1) nm as determined from 50 measurements). Additional pseudo-hexagonal platelets were chosen for DF imaging and produced similar results. Lattice fringes are difficult to see in the HR-TEM images (Figures 2g, i, j, l) but weak FFT spots are present (Figures 2h, k). FFT patterns calculated from whole HR-TEM images (e.g. inset in Figure 2g) matched the SAED patterns well. When comparing FFTs from different areas of the particle, the reflections represented by the brightest spots were slightly different (Figures 2h, k), though they were aligned, meaning that different areas of the particle were tilted with respect to each other. Semi-quantitative analysis of the EDS spectrum (Figure 2m) gave an atomic Fe/S ratio of 14, which is higher than typically reported values of sulfate green rust that range from 4.5-6 for the structural formulas considered here (Simon et al. 2003; Christiansen et al. 2009). A significant Si peak is also present, along with a trace amount of Zn, very similar to what was reported for other green rust particles in Johnson et al. (2014).

Green-rust pseudo-hexagonal platelets were also found downstream in the sediment at the mine drainage terrace site, shown here in Figure 3. Having been exposed to atmospheric oxygen more than the particles in the outflow site (Figure 2), these platelets may have oxidized to ferric green rust while keeping their basic morphology, but they still show characteristics very similar to the platelets found at the groundwater outflow site. Smaller aggregates of unidentified iron oxides were commonly found on the surface of the platelets (dark areas on the platelets in Figures 3a, b). SAED patterns of the sediment platelets (Figure 3c) can be indexed in the same way as platelets from the outflow, based on the green rust structure *P*-31$\bar{m}$ {note: minus sign is overbar} and [001] zone axis orientation, and the general particle size and morphology are also

similar. DF imaging (Figures 3d-f) of particular hkl reflections (circled in Figure 3c) also clearly show bright areas a few nanometers in diameter, indicating that these are not coherent single crystals, similar to those seen in Figure 2. The iron oxide precipitates on the surface of the platelet (dark areas in Figure 3a) do not contribute to the primary hexagonal SAED pattern (Figure 3c) and do not light up during DF imaging using those particular reflections. HR-TEM shows a crystalline area with amorphous patches (Figures 3g, h) but not all areas look like this one. Similarly to the outflow platelets, FFTs from different areas of the particle are aligned but some areas of the particle are tilted with respect to each other (data not shown). S is only present in trace amounts and the Fe/S atomic ratio calculated from the EDS spectrum is 58.5. Also present in trace amounts are the metals Ni and Cu, not previously found on these types of particles at the anoxic mine drainage outflow site (Johnson et al. 2014). The Cu signal is not from the grid mesh, which is made of Au, nor the sample holder, which is made of Be.

Synthetic green rust

GR-SO_4 was successfully produced under a variety of conditions using four synthesis procedures (Table 1). Photos showing the color changes during synthesis reactions from transparent yellow-orange to opaque dark olive green during titrations or fast addition of NaOH to initial Fe^{II}/Fe^{III} solutions (starting pH 1.5-3.0 depending on reagent brands used) are shown in Supplemental Figure S1). During titrations, when NaOH solution was added drop-wise with rapid mixing until a pH between 7 and 8, the sudden locally-high pH caused dark precipitates to form that eventually dispersed or dissolved as the solution equilibrated at lower pH. Over months of time, the solutions equilibrated at a pH of approximately 5-6 under anoxic conditions.

XRD data are shown for each synthesis in Figure 4 and Table 3. Green rust was the predominant product, and only minor amounts of magnetite and/or amorphous silica are present. Material sampled either immediately or within 1-2 days exhibited the sharp diffraction peaks of GR-SO_4 (001), (002), and (003) planes, and they appeared to be very stable over many months when stored anoxically. The only exception to the stability was GR-D, which transformed to goethite and magnetite. This was likely because the final product in the reaction vessel was in close proximity to an orange oxidized layer at the surface of the reaction solution and that nFe^{II}/nFe^{III} was close to 1 instead of 2. The crystallite sizes perpendicular to each hkl plane, calculated using the Scherrer equation with $K = 1$, are shown in Table 4. The averages (with standard deviations) over all sulfate green rust peaks in each sample were 24(9) (GR-A), 25(12) (GR-B), 28(7) nm (GR-C), and 18(5) nm (GR-D). The average crystallite sizes for just the 001, 002 and 003 peaks (corresponding approximately the particle thickness if it is only one crystallite thick) are 26(2) nm (GR-A), 26(2) nm (GR-B), 27(2) nm (GR-C), and 15(1) nm (GR-D).

In the following paragraphs, we will discuss the results from the nanoscale characterization of the four synthetic green rust products by analytical TEM. A comparison of crystallographic d-spacings measured using XRD, SAED and FFT is presented in Table 3, and Fe/S atomic ratios calculated from EDS spectra are shown in Table 5.

Synthesis GR-A primarily produced GR-SO_4 with a minor amorphous silica component, as shown by XRD in Figure 4 and Supplemental Figure S4. During the synthesis, the NaOH solution was titrated into the initial Fe^{II}-Fe^{III} solution under the conditions listed in Table 1. Samples for XRD were taken at different pHs during the titration, and while green rust was dominant at pH 7, at pH 7.5 and 8 another clay was present (matching the pattern for corrensite; data not shown). However, after aging the pH 8 sample for two days, the XRD pattern once

again matched green rust. The explanation for this is not known, but it is mentioned here because the fresh pH 8 sample was used for further analysis and some green rust platelets were found. These pseudo-hexagonal platelets (Figures 5a, b), exhibited diffuse reflections in the SAED pattern (Figure 5c) that are identical (both in arrangement and d-spacing) to those of the natural green rust platelets. The sharper spots in the SAED pattern belong to the crystalline nanoparticles deposited on the surface of the platelets, as confirmed by DF imaging (Figure 5f). These crystalline nanoparticles are referred to as "np's" in Table 3, to distinguish them from nanorods, because goethite nanorods (identified by SAED) were also present on the surface of the platelets. DF imaging revealed that the platelets are polycrystalline, which was confirmed by HR-TEM imaging where patches of crystalline and amorphous areas are visible. The area in Figures 5g, h, however, exhibits mostly uniform lattice fringes and the FFT pattern (Figure 5i) shows the typical hexagonal spot pattern that matches the SAED pattern for this particle. The dark particle on the platelet surface does not diffract at this orientation. Compositionally, GR-A matches the theoretical GR-Na,SO_4 well with an Fe/S atomic ratio of 4.4 (4.5 for GR-Na,SO_4), and a Na peak. A significant Si peak is also present, and the reasons for this will be given in the discussion section.

GR-SO_4 was also the dominant product of synthesis GR-B, with minor amounts of magnetite and amorphous silica, and the sample was stable for many months (Figure 4). However, GR-B produced platelets that were distinctly different in morphology from GR-A (Figure 6). Instead of fairly regular hexagonal platelets, polygons of varying edge lengths and interior angles of 60° and/or 120° were also found, such as parallelograms and triangle-like hexagons (alternating long and short sides) (see Figure 6k). These platelets have rims that were thicker than the centers (as confirmed by SEM in Figure 6m). The platelet thickness is

368 approximately 3-5 nm because the contrast difference between the particles and the underlying
369 ultrathin (3-4 nm) carbon film is very small, even though the particle is crystalline and composed
370 of heavier elements. Differences in diffraction contrast were also very helpful in order to
371 understand the intriguing polycrystalline nature of these platelets, which have a dendritic pattern
372 starting near the center of the particles and going outward towards the edges (best seen in Figure
373 6d). Diffraction contrast causes the crystalline areas to appear darker, even in the low
374 magnification images. The dendritic features are composed of nanocrystallites that are aligned
375 along short dendritic segments, but are slightly rotated with respect to each other between
376 neighboring dendrite areas (Figure 7). DF imaging (Figures 6e,f) was used to confirm that the
377 platelets are composed of nanocrystalline areas mixed with amorphous areas, and that areas that
378 appear bright do correspond directly to the crystalline dendritic patterns observed in low
379 magnification and HR-TEM images. Both DF images were taken from the hkl reflections
380 indicated by circles in the hexagonal SAED pattern in Figure 6c. The Fe/S atomic ratio of the
381 thin platelets is 7, and as with GR-A platelets, there is a prominent Si peak.
382 The sharp diffraction spots in Figure 6c belong to the highly crystalline magnetite
383 nanoparticles on the surface of the GR-SO_4 platelets. Aggregates of magnetite nanoparticles
384 (individual particles ranging in size from a few to a few tens of nanometers in diameter)
385 dominated the TEM grids and seemed much more prevalent than green rust platelets in syntheses
386 GR-B and GR-C. These magnetite particles have uniform lattice fringes extending to their edges.
387 Some have a hexagonal morphology, but a cube of magnetite in an [111] orientation can appear
388 hexagonal. Differentiating green rust from individual magnetite particles using HR-TEM and
389 FFT was problematic because their crystallographic planes have d-spacings that are too close to
390 distinguish from each other, including around the characteristic reflection for magnetite at 4.8 Å.

The XRD spectra for GR-B, as well as the other synthetic samples (Figure 4), consistently included very intense GR-SO_4 peaks and only small magnetite peaks, so sampling for this particular TEM grid preparation may have played a role in the observed dominance of the magnetite nanoparticles over the large platelets. The EDS Fe/S atomic ratio for the magnetite nanoparticles is 142 (there is only a trace amount of S), and there is only a small Si peak for these particles as compared to the platelets.

Surprisingly, there was no obvious difference between the GR-B synthesis (performed under oxic conditions) and GR-C, a completely anoxic synthesis. Both syntheses had identical XRD patterns (Figure 4), and both had many aggregates of magnetite nanoparticles. In a sample of GR-C aged 80 days, platelets virtually identical to those in GR-B (aged 54 days) were observed with the same characteristics: various types of six-sided polygons, only a few nm in thickness, dendritic contrast patterns, and rims that were thicker than the center (data not shown). Therefore, we infer that the presence of dissolved oxygen during the addition of NaOH is neither detrimental nor necessary. The products of both of these syntheses, stored anoxically, are very stable long-term.

Unlike the other syntheses described so far in this study and in the published literature, GR-D produced green rust particles of nanorod morphology, approximately 5-10 nm in diameter and a few tens of nanometers in length (Figure 8), with a Fe/S atomic ratio of 56. Nanorods are not currently a known morphology of sulfate green rust, which is typically found as thin pseudo-hexagonal platelets up to a few micrometers in diameter. The XRD spectrum of fresh GR-D clearly shows GR-SO_4, as well as an amorphous (iron oxide?) component, but SAED was not conclusive due to the lack of the GR-SO_4 (001) or (002) reflections. The unusual morphology was reason enough to get direct confirmation by HR-TEM that the nanorods were GR-SO_4 and

not goethite, which has been previously reported as a GR-SO_4 precursor (Ahmed et al. 2010). Nanorods viewed from the side did not provide any characteristic d-spacing values to identify the structure, so we focused on the dark, diamond-shaped particles (circled in Figure 8a) on the assumption that they were the cross-sectional view of the nanorods. Indeed, HR-TEM and corresponding FFT of one of those diamond-shaped particles exhibited the characteristic interlayer d-spacing of the (001) plane as shown in Figure 8d. More examples are shown in Supplemental Figure S2. The FFT pattern in Figure 8e exactly matches the simulated electron diffraction pattern of sulfate green rust (structure identified by Simon et al. 2003) oriented on the [100] zone axis (Figure 8f). Moiré fringes from adjacent parallel planes were also considered, but ruled out by calculating the expected moiré fringe spacing *D* from the d-spacings of adjacent areas (d_1, d_2) using the equation $D = \frac{d_1 * d_2}{d_1 - d_2}$ (Edington 1975). The calculated *D* is 8.6 Å, while the d-spacings measured directly from the HR-TEM image and from the FFT pattern are 10.0-10.6 Å which are reasonably close (within error) to the diagnostic (001) spacing of green rust (d = 11 Å). D-spacings from the SAED of nanorod aggregates also support the conclusion that these particles are not other iron (oxyhydr)oxide mineral phases such as goethite or magnetite, because characteristic reflections of those minerals are missing.

DISCUSSION

Morphology

Natural green rust minerals found in the outflow and sediment of Ronneburg mine drainage (Johnson et al. 2014, and this study) are typically pseudo-hexagonal platelets with rounded corners, likely in various stages of dissolution. Pseudo-hexagons are the characteristic

morphology of green rust (Géhin et al. 2002; Skovbjerg et al. 2006; Trolard et al. 2007; Christiansen et al. 2009; Usman et al. 2012). An unexpected result of this research was the synthesis of three morphologically different sulfate green rusts: pseudo-hexagonal platelets, four- to six-sided polygonal platelets with interior angles of 60° and/or 120°, and nanorods. The pseudo-hexagons of synthesis GR-A look the most similar to the outflow and sediment green rust particles in the Ronneburg mine drainage. The polygons of GR-B (and GR-C, not shown) are quite variable, and have an even larger aspect ratio with thicknesses of approximately 3-5 nm and diameters of up to a few micrometers. GR-D produced nanorods, which are not a known morphology of green rust though there is no reason to believe that we will never find them in nature. It is quite common for minerals to exhibit a wide variety of morphologies when formed in nature and in the laboratory.

In order to produce these different morphologies, particularly the nanorods in GR-D, different synthesis conditions and reaction kinetics are likely important factors. For GR-D the Fe^{II}/Fe^{III} ratio was less than half of the stoichiometric ratio used for GR-B and GR-C, resulting in an excess of Fe^{III}, and the total Fe concentration was about 50% lower. The molar ratio of OH^-/Fe_{total} for GR-D was half of that for the other three syntheses. These ratios are thought to be the determining factor for which mineral phase forms (e.g. green rust, goethite, or magnetite) (Ruby et al. 2006). Kinetics determined by the rate of addition of base, either by slow titration over many hours or merely dumped in all at once, may have also played a role in the determination of morphology. A more systematic study is necessary, and recommended, in order to understand which specific variable(s) are responsible for these morphological differences.

Polycrystallinity and coherency

In a coherent, textured, polycrystalline particle the individual crystallites will be well aligned, while in an incoherent particle there are a significant amount of crystalline defects and misaligned crystallites. The broad, diffuse spots in the SAED patterns give the first clues that the crystallites may be slightly misaligned, though this broadening could also be due to the inherent strain and incoherency within nano-sized crystallites (Waychunas 2001).

The crystallite sizes calculated from the XRD peak broadening vary depending on the hkl plane. For example, GR-A and GR-B have a calculated crystallite size of 9 and 4 nm (respectively) perpendicular to the (111) plane, but a size of 24 nm perpendicular to the (001) plane. The bright spots on the DF images are only a few nanometers in diameter. If the crystallite shape is an elongated cylinder oriented perpendicular to the (001) plane, it would explain why the size calculated using the (111) plane is smaller and closer to the size of the bright spots in the DF images. However, it is difficult to explain why the crystallite sizes calculated from the (001) plane for GR-B and GR-C were 24 nm, while the particles appeared to only be a few nanometers thick (see Results section above). The crystallite sizes calculated using the Scherrer equation with the (001) plane of sulfate green rust in other studies were similar: 40 nm (Guilbaud et al. 2013), 36-47 nm (Ayala-Luis et al. 2008), and 5-30 nm depending on Fe^{II}/Fe^{III} and different synthesis methods (Mazeina et al. 2008).

The mosaics of brightly-imaged spots observed by DF-TEM provide conclusive evidence of the incoherent nature of the natural and synthetic green rust platelets. The crystallites must be somewhat, although not exactly aligned, yet dark areas exist that represent other diffraction conditions. However, it is not immediately obvious why this can occur but at the same time have SAED patterns that do not show significant crystallite rotation. One explanation for this could be that some crystallites (i.e. GR-B in Figure 7b) are tilted such that only one or two pairs of

diffraction spots are visible. Tilting perpendicular to a specific lattice plane by approximately 4-10° causes other diffraction spots to completely disappear from the SAED pattern, without new spots appearing (see Figure 9). It is also possible that the low contrast areas are amorphous. It is unlikely that all the crystallites would be aligned if each were completely surrounded by amorphous material, unless the amorphous regions are artifacts of oxidation by air. Nevertheless, they could be connected by minute bridges that would be difficult to observe even in thin green rust sheets.

Implications for particle formation

Our understanding of mineral formation mechanisms is incomplete, and green rust is no exception, though there are some theories based on X-ray diffraction data. Guilbaud et al. (2013) proposed that GR-SO_4 growth was driven by Ostwald ripening, because the evolution of the crystallite size (calculated from the (001) plane peak broadening in the XRD spectra) matched the predicted curve for the Ostwald ripening model. Using wide angle X-ray scattering (WAXS) to perform an in situ, time-resolved analysis of GR-SO_4 formation using procedures similar to those in this study, Ahmed et al. (2010) proposed that the interaction between aqueous Fe^{2+} and goethite above pH 7 resulted in Fe^{II}/Fe^{III} hydroxide sheets with the brucite structure, equivalent to the hydroxide layers of green rust. As hydrolysis of Fe^{2+} proceeds, the GR-SO_4 sheets will continue to grow along the (001) plane (Ahmed et al. 2010).

The existence of 2-nm crystalline domains assembled in imperfect ways along the (001) plane, such as we see in the natural green rusts and synthetic GR-A, GR-B and GR-C described in this study, is evidence that the building blocks for these platelets are nanoparticles. These nanoparticles may have formed from molecular clusters containing Fe^{II}, Fe^{III}, O, and possibly

506 SO_4^{2-} and Si. Known polymers that can be stable in acidic conditions include polyferric sulfate
507 and polyferric silicate sulfate (Zouboulis and Moussas 2008). Regardless of how the
508 nanoparticles formed, and if they were part of other iron oxides such as schwertmannite or
509 goethite prior to forming green rust (Ahmed et al. 2010), they ultimately aggregated in more or
510 less oriented fashion. Different surface energies on each crystallographic face or part of the
511 particle surface will affect how each crystallite orients itself with respect to its neighbors
512 (Waychunas 2001). Presumably the layered double hydroxide structure of green rust does not
513 allow many ways for those different faces to align.
514 In the case of GR-B (Figures 6, 7, and similarly GR-C), the dendrite patterns are
515 composed of nanocrystallites that are oriented along single dendrite strands, with amorphous
516 silica in-between the strands (Supplementary Figure S3). Some areas are tilted with respect to the
517 others (even if one pair of spots aligns well with those in other FFTs) (Figure 7). True dendritic
518 crystal growth is not likely because dendrite formation typically involves rapid crystallization
519 (atom-by-atom) and limited solution flow (Waychunas 2001). GR-B suggests a mechanism of
520 aggregation into a dendrite-like pattern, not atom-by-atom growth. Comparing strands, the
521 crystallites are slightly rotated with respect to each other. This could occur if, for example, two
522 crystallites attached side-by-side, but there was a dislocation at the grain boundary due to
523 incomplete hydrolysis of inward-facing –OHs or Si on the surface of the nanoparticle. That
524 dislocation could have propagated and other crystalline strands may have branched off at
525 dislocations and misalignments of crystallites. Nevertheless, it is difficult to explain why such a
526 pattern would end up creating a hexagon shape. A possible argument against oriented attachment
527 for GR-B is that one particle in Figure 6k looks like it could have formed via spiral growth,

528 which is typically thought to form by attachment of single atoms and not nanoparticles or
529 clusters.

530 The natural green rusts found in the outflow water and terrace sediment at the Ronneburg
531 mine drainage site, and synthesis product GR-A, are also polycrystalline with crystallites only a
532 few nanometers in size in directions along the width of the platelets. However, it is more difficult
533 to explain the relationship between the crystallites because there is not a clear pattern, unlike the
534 dendrite patterns in GR-B and GR-C. If we consider the platelet in the outflow water shown in
535 Figure 2, there are distinct regions of many bright spots close to each other, and overall darker
536 regions. When the DF images from the three chosen hkl reflections (030, -330, -300) {note to
537 typesetter: minus signs are overbars} are overlain, nearly the entire particle is covered in bright
538 spots although there are still some small dark areas in-between. Because some spots are bright in
539 only one or two DF images, and some in all three, we can infer that this particle is composed of
540 crystallites that are tilted (but not rotated more than a couple of degrees) with respect to each
541 other. There are amorphous areas as well. The green rust platelet from the terrace sediment
542 shown in Figure 3 similarly has large regions that appear bright when a particular hkl reflection
543 is chosen. However, these regions are more distinct than for the outflow platelet and few spots
544 appear bright in more than one DF image. This could mean that larger sections of the particle,
545 many tens of nanometers in size, are tilted with respect to each other, and the crystallites within
546 each region are more closely aligned (the platelet is not flat). Again, there are still dark areas
547 between the bright spots that could be amorphous material.

548 The features we see in both the synthetic and natural green rust platelets cannot be
549 explained by classical crystal growth mechanisms. Instead, non-classical growth mechanisms
550 rely on building blocks of molecules, clusters, and nanoparticles to aggregate in

crystallographically-compatible ways to form larger particles that may diffract as single crystals but contain grain boundaries and defects. Oriented aggregation is an example of this, with nanoparticle building blocks such as ferrihydrite forming goethite nanorods (Banfield et al. 2000; Penn et al. 2006), and hematite nanoparticles stabilized by acetate ligands forming two-dimensional hematite platelets (Cai et al. 2014). In an even more complex variation, often found in biomineralization, building blocks of inorganic material can assemble with organic or inorganic polymers in oriented ways to form mesocrystals, which diffract like single crystals but have complex domains (Cölfen and Mann 2003; Cölfen and Antonietti 2005). Nacre, a calcium carbonate mesocrystal structure produced by bivalves, has been shown by DF imaging to be composed of nano-domains of aragonite that are oriented in the same direction, despite being surrounded by a contiguous organic matrix (Rousseau 2011). Even though oriented aggregation is a possible formation mechanism for the green rusts in this study, particle formation here may be more likely a combination of oriented aggregation and atom-by-atom coarsening (Xue et al. 2014). Also known as Ostwald ripening, atom-by-atom coarsening is particle growth by the addition of individual atoms, when larger particles grow at the expense of smaller ones (Ostwald 1897; Banfield and Zhang 2001).

Although the platelets from the outflow water in Figure 1 were not imaged using dark-field microscopy, the HR-TEM images show features that are different than the other natural green rust platelets in Figures 2 and 3, as well as the synthetic green rusts. FFT patterns calculated from smaller regions of the image are well aligned with each other, and parallel lattice fringes are clearly visible throughout the image, even through the light-colored patches. Therefore, this particle exhibits more coherency than the others.

574 **Silicon association with green rust**

575 Silicon commonly associates with iron oxides in natural systems. For example, amorphous silica
576 was found intimately associated with schwertmannite nanoneedles in a mine drainage system
577 (French et al. 2012) and on ferrihydrite precipitates of Fe-bearing spring waters (Carlson and
578 Schwertmann 1981). The poorly-crystalline iron oxide particles, found in mine drainage water
579 and sediments of the Ronneburg uranium described in our previous study (Johnson et al. 2014)
580 were also associated with Si, and the green rust platelets were no exception. However, the
581 concentration of Si (0.4 mM at 12°C) in the drainage water (Johnson et al. 2014) was under-
582 saturated with respect to amorphous silica (solubility of 1.5 mM (Gunnarsson and Arnorsson
583 2000)). Although the concentration that we observed is within the normal range of dissolved Si
584 in natural waters (0.1-1.2 mM) (Burton and Johnston 2012), one might estimate this it is unlikely
585 that Si would precipitate or sorb to the iron oxide particles. However, it has been shown
586 numerous times that iron oxides have a high affinity for silicate sorption in natural waters (e.g.
587 Carlson and Schwertmann 1981, 1987; Sun et al. 2012) and soils (e.g. Childs 1992). Silicic acid
588 (H_4SiO_4) in solution can sorb to ferrihydrite and polymerize (Swedlund et al. 2009), resulting in
589 solid-phase Si/Fe ratios comparable to those found by TEM EDS in this study. The affinity of
590 silicate for other ferric minerals can vary widely. For example, the solid phase Si/Fe ratios for
591 goethite following the sorption of H_4SiO_4 (Hiemstra et al. 2007) were an order of magnitude
592 lower than for ferrihydrite in the Swedlund et al. (2009) study.

593 We were unable to remove Si entirely from our synthetic system and noticed a high
594 affinity of the synthetic green rust for Si, similar to the natural green rust particles. Si/Fe ratios of
595 nanorods and magnetite nanoparticles were much less than for synthetic green rust platelets. The
596 synthetic green rusts concentrated the trace amounts of Si that were originally present in the

starting materials and solutions. This was determined by comparing the Si/Fe ratios of the original solution (determined by inductively-coupled plasma atomic emission spectroscopy, ICP-AES), and EDS spectra of the lacey carbon film of the TEM grid and green rust platelets (data not shown). The Si/Fe ratios for the green rust platelets were much higher than for the lacey carbon and in solution. Ultimately, we determined that our anoxic water (boiled and stored in borosilicate glass containers) was the most likely source of silica contamination because that boiled water applied to a TEM grid did give a Si peak using EDS, but no Si was present on a grid prepared with water that had only been stored in plastic. Using Si-free synthesis vessels and tubing did not solve the problem. EDS of ~ 1 nm diameter spot size in scanning TEM (STEM) mode was used to compare the Si/Fe ratios of bright (corresponding to crystalline "dendrite patterned" areas of GR-B) and dark areas of a green rust platelet (Supplemental Figure S3). Dark areas had a higher Si/Fe compared to bright areas, confirming that (amorphous) Si is enriched in-between the crystallites. Another piece of evidence for the presence of significant amounts of Si associated with the platelets are the very broad and weak diffraction peaks (15-25 °2Θ, centered around 20°), which are indicative of amorphous silica. These were seen in all XRD spectra of green rust syntheses, with the exception of GR-D. These peaks are not visible in Figure 4, but are clear when the diffraction patterns are enlarged (Supplemental Figure S4).

Since Si was present in the starting solution (at concentrations of 1-2 μM), it could potentially sorb onto the crystallites during or after the aggregation process. There was no evidence in the synthetic green rusts of the surface "patchiness" seen in the natural green rust platelets in Figure 1 and Johnson et al. (2014).

Comparison to other synthetic green rusts

The sulfate green rusts produced in this study show differences to those in the published literature, at least visually, particularly for GR-B which was synthesized with the same method as Ruby et al. (2003). Synthetic green rust products, whether abiotic or biotic, usually have fairly sharp corners and straight edges, though the size and morphology varies widely even within a sample (Ruby et al. 2003; Skovbjerg et al. 2006; Ahmed et al. 2010; Usman et al. 2012). GR-B platelets with rims did look strikingly similar to green rust in the process of reacting with Cr^{VI} (Skovbjerg et al. 2006). In that study, not only were thicker rims visible, but also the center of the platelet seemed to dissolve away with the formation of secondary products (goethite). Dissolution of the inner platelet, leaving the rims basically intact, was also observed in the GR-B sample aged for 90 days (Supplemental Figure S5). However, in the case of green rust reacting with Cr^{VI}, the starting material was well-faceted, smooth platelets (Skovbjerg et al. 2006), unlike what we observed in GR-B. Structurally, it was difficult to compare d-spacings to published work because that data is not often reported in conjunction with the SAED pattern, though the typical hexagonal spot pattern (oriented down the [001] axis) was consistently present.

IMPLICATIONS

As we show in this study, both natural and synthetic green rust minerals exhibit an extraordinary complexity in structure and composition on the nanoscale. Detailed TEM analyses reveal the polycrystalline nature of these nanometers-thin platelets, filled with defects that result in many reactive sites and, likely, atomically rough surfaces. These properties, combined with the presence of both Fe^{II} and Fe^{III} in the layered-double-hydroxide structure and nanoscale thinness that results in a platelet having a high surface to volume ratio, help explain why this elusive phase has a remarkable potential for participating in the reactions of environmental systems.

643 Supplemental Figure S6 presents an overview of how green rusts participate in the iron cycle,
644 with dissolution and precipitation reactions happening both biotically and abiotically. At the
645 Ronneburg mine drainage site, the outflowing water and adjacent creek is highly enriched in
646 both Fe(III)-reducing and Fe(II) oxidizing bacteria (Fabisch et al. 2013, Fabisch et al. 2015 in
647 review) that likely participate in these reactions.

648 Trace metal contaminant cycling is also coupled to iron cycling. At the former uranium
649 mine (Johnson et al. 2014 and this study), we found that green rust platelets can contain trace
650 amounts of Zn, Ni and Cu, metals which were prevalent in the outflowing waters discharging
651 directly from the underground mine workings. Carbonate green rust formation from ferrihydrite
652 has indirectly been found to enhance Ni uptake in a ferruginous lake (Zegeye et al. 2012), but we
653 believe this is the only other study to date that has reported trace metal association with green
654 rust from a natural system. In addition to metals, green rust appears to have a strong affinity for
655 Si, which is also commonly present in ground- and surface waters. Si that interacts with the
656 particle during formation or during its lifetime could impact green rust reactivity in ways that are
657 not fully understood. It would be beneficial to seek out and carefully sample, preserve, and
658 characterize by analytical TEM green rust minerals in a variety of environments.

659 When performing laboratory experiments using mineral nanoparticles and extrapolating
660 the results to environmental relevance, there are many steps one can take to make experimental
661 systems more representative in their complexity. In addition to using natural matrices (i.e. natural
662 waters, soil or sediments) and environmentally-relevant concentrations of reactants (Vignati et
663 al. 2007), it is helpful to synthesize materials that have a similar morphology, nanoscale
664 structure, and composition as the natural materials of interest. In this particular study, we show
665 that some of our synthetic sulfate green rust products did have a remarkable similarity to the

green rusts found in the mine drainage water and sediment of our field site, including polycrystalline, incoherent structures and association with silica. We suggest that these attributes will make a significant difference in their reactivity with pollutants and during biogeochemical iron cycling.

Careful anoxic sample collection, preparation, and storage should someday allow us to finally understand the true extent and importance of green rust phases and their variations in nature. We anticipate that in the future, green rust will be shown to be widespread and highly active in a wide variety of suboxic to anoxic critical zone habitats.

SUPPLEMENTAL MATERIAL

Supporting information contains figures showing color changes during synthesis, additional TEM data and enlarged XRD spectra and can be accessed at http://www.minsocam.org/MSA/AmMin/toc.

ACKNOWLEDGEMENTS

Carol A. Johnson was financially supported by the National Science Foundation (NSF) Integrative Graduate Education and Research Traineeship program (grant DGE-0504196), and the NSF and the Environmental Protection Agency (EPA) through the Center for the Environmental Implications of NanoTechnology (CEINT) (NSF Cooperative Agreement EF-0830093). The Institute for Critical Technology and Applied Science (ICTAS) Nanoscale Characterization and Fabrication Laboratory provided access to and technical support for the electron microscopes. Chris Winkler was particularly helpful in this regard. We also thank Gina Freyer and Maria Fabisch (Friedrich Schiller University Jena, Germany) for collaboration on the

fieldwork and broader project, and J. Donald Rimstidt (Virginia Tech) for valuable discussions and feedback on this manuscript.

REFERENCES

Ahmed, I.A.M., Benning, L.G., Kakonyi, G., Sumoondur, A.D., Terrill, N.J., and Shaw, S. (2010) Formation of green rust sulfate: a combined in situ time-resolved X-ray scattering and electrochemical study. Langmuir, 26, 6593–6603.

Ayala-Luis, K.B., Koch, C.B., and Hansen, H.C.B. (2008) The standard Gibbs energy of formation of Fe(II)Fe(III) hydroxide sulfate green rust. Clays and Clay Minerals, 56, 633–644.

Banfield, J.F., and Zhang, H. (2001) Nanoparticles in the Environment. In J.F. Banfield and A. Navrotsky, Eds., Nanoparticles and the Environment Vol. 44, pp. 1–58. Mineralogical Society of America, Chantilly, Virginia.

Banfield, J.F., Welch, S.A., Zhang, H., Ebert, T.T., and Penn, R.L. (2000) Aggregation-based crystal growth and microstructure development in natural iron oxyhydroxide biomineralization products. Science, 289, 751–754.

Bearcock, J.M., Perkins, W.T., Dinelli, E., and Wade, S.C. (2006) Fe(II)/Fe(III) "green rust" developed within ochreous coal mine drainage sediment in South Wales, UK. Mineralogical Magazine, 70, 731–741.

Burton, E.D., and Johnston, S.G. (2012) Impact of silica on the reductive transformation of schwertmannite and the mobilization of arsenic. Geochimica et Cosmochimica Acta, 96, 134–153.

Cai, J., Chen, S., Ji, M., Hu, J., Ma, Y., and Qi, L. (2014) Organic additive-free synthesis of mesocrystalline hematite nanoplates via two-dimensional oriented attachment. CrystEngComm, 16, 1553–1559.

Caraballo, M.A., Michel, F.M., and Hochella Jr., M.F. (2015) The rapid expansion of environmental mineralogy in unconventional ways: Beyond the accepted definition of a mineral, the latest technology, and using nature as our guide. American Mineralogist, 100, 14–25.

Carlson, L., and Schwertmann, U. (1981) Natural ferrihydrites in surface deposits from Finland and their association with silica. Geochimica et Cosmochimica Acta, 45, 421–429.

——— (1987) Iron and manganese oxides in Finnish ground water treatment plants. Water Research, 21, 165–170.

721 Childs, C.W. (1992) Ferrihydrite: A review of structure, properties and occurrence in relation to
722 soils. Zeitschrift für Pflanzenernährung und Bodenkunde, 155, 441–448.

723 Christiansen, B.C., Balic-Zunic, T., Petit, P.-O., Frandsen, C., Mørup, S., Geckeis, H.,
724 Katerinopoulou, A., and Stipp, S.L.S. (2009) Composition and structure of an iron-bearing,
725 layered double hydroxide (LDH) – Green rust sodium sulphate. Geochimica et
726 Cosmochimica Acta, 73, 3579–3592.

727 Christiansen, B.C., Balic-Zunic, T., Dideriksen, K., and Stipp, S.L.S. (2009) Identification of
728 green rust in groundwater. Environmental Science & Technology, 43, 3436–3441.

729 Cölfen, H., and Antonietti, M. (2005) Mesocrystals: Inorganic superstructures made by highly
730 parallel crystallization and controlled alignment. Angewandte Chemie, 44, 5576–91.

731 Cölfen, H., and Mann, S. (2003) Higher-order organization by mesoscale self-assembly and
732 transformation of hybrid nanostructures. Angewandte Chemie (International ed. in English),
733 42, 2350–65.

734 Dong, H., and Lu, A. (2012) Mineral-microbe interactions and implications for remediation.
735 Elements, 8, 95–100.

736 Edington, J.W. (1975) Practical Electron Microscopy in Materials Science. Monograph 3:
737 Interpretation of Transmission Electron Micrographs. MacMillan Press, Ltd, London.

738 Erbs, M., Hansen, H.C.B., and Olsen, C.E. (1999) Reductive dechlorination of carbon
739 tetrachloride using iron(II) iron(III) hydroxide sulfate (green rust). Environmental Science
740 & Technology, 33, 307–311.

741 Fabisch, M., Beulig, F., Akob, D.M., and Küsel, K. (2013) Surprising abundance of Gallionella-
742 related iron oxidizers in creek sediments at pH 4.4 or at high heavy metal concentrations.
743 Frontiers in Microbiology, 4, 1–12.

744 French, R.A., Caraballo, M.A., Kim, B., Rimstidt, J.D., Murayama, M., and Hochella Jr, M.F.
745 (2012) The enigmatic iron oxyhydroxysulfate nanomineral schwertmannite: Morphology,
746 structure, and composition. American Mineralogist, 97, 1469–1482.

747 Géhin, A., Ruby, C., Abdelmoula, M., Benali, O., Ghanbaja, J., Refait, P., and Génin, J.-M.R.
748 (2002) Synthesis of Fe(II-III) hydroxysulphate green rust by coprecipitation. Solid State
749 Sciences, 4, 61–66.

750 Génin, J.-M.R., Ruby, C., Géhin, A., and Refait, P. (2006) Synthesis of green rusts by oxidation
751 of Fe(OH)2, their products of oxidation and reduction of ferric oxyhydroxides; –pH
752 Pourbaix diagrams. Comptes Rendus Geoscience, 338, 433–446.

753 Guilbaud, R., White, M.L., and Poulton, S.W. (2013) Surface charge and growth of sulphate and
754 carbonate green rust in aqueous media. Geochimica et Cosmochimica Acta, 108, 141–153.

Gunnarsson, I., and Arnorsson, S. (2000) Amorphous silica solubility and the thermodynamic properties of H4SiO4° in the range of 0° to 350°C at Psat. Geochimica et Cosmochimica Acta, 64, 2295–2307.

Han, Y.-S., Hyun, S.P., Jeong, H.Y., and Hayes, K.F. (2012) Kinetic study of cis-dichloroethylene (cis-DCE) and vinyl chloride (VC) dechlorination using green rusts formed under varying conditions. Water Research, 46, 6339–6350.

Hanawalt, J.D., Rinn, H.W., and Frevel, L.K. (1938) Chemical analysis by X-ray diffraction -- Classification and use of X-ray diffraction patterns. Industrial & Engineering Chemistry, Analytical Edition, 10, 457–512.

Hiemstra, T., Barnett, M.O., and van Riemsdijk, W.H. (2007) Interaction of silicic acid with goethite. Journal of Colloid and Interface Science, 310, 8–17.

Hochella Jr, M.F., Aruguete, D., and Kim, B. (2012) Naturally occurring inorganic nanoparticles: General assessment and a global budget for one of Earth's last unexplored major geochemical components. In A.S. Barnard and H. Guo, Eds., Nature's Nanostructures pp. 1–31. Pan Stanford Pte Ltd.

Johnson, C.A., Freyer, G., Fabisch, M., Caraballo, M.A., Küsel, K., and Hochella Jr., M.F. (2014) Observations and assessment of iron oxide and green rust nanoparticles in metal-polluted mine drainage within a steep redox gradient. Environmental Chemistry, 11, 377–391.

Jönsson, J., and Sherman, D.M. (2008) Sorption of As(III) and As(V) to siderite, green rust (fougerite) and magnetite: Implications for arsenic release in anoxic groundwaters. Chemical Geology, 255, 173–181.

Jorand, F.P.A., Sergent, A.-S., Remy, P.-P., Bihannic, I., Ghanbaja, J., Lartiges, B., Hanna, K., and Zegeye, A. (2013) Contribution of anionic vs. neutral polymers to the formation of green rust 1 from γ-FeOOH bioreduction. Geomicrobiology Journal, 30, 600–615.

Klug, H.P., and Alexander, L.E. (1974) X-Ray Diffraction Procedures for Polycrystalline and Amorphous Materials, 2nd ed., 618-708 p. John Wiley & Sons, New York.

Kukkadapu, R.K., Zachara, J.M., Fredrickson, J.K., and Kennedy, D.W. (2004) Biotransformation of two-line silica-ferrihydrite by a dissimilatory Fe(III)-reducing bacterium: Formation of carbonate green rust in the presence of phosphate. Geochimica et Cosmochimica Acta, 68, 2799–2814.

Lavina, B., Dera, P., and Downs, R.T. (2014) Modern X-ray diffraction methods in mineralogy and geosciences. In G.S. Henderson, D.R. Neuville, and R.T. Downs, Eds., Spectroscopic Methods in Mineralogy and Materials Science Vol. 78, pp. 1–31. Reviews in Mineralogy and Geochemistry, Mineralogical Society of America, Chantilly, Virginia.

Mazeina, L., Navrotsky, A., and Dyar, D. (2008) Enthalpy of formation of sulfate green rusts. Geochimica et Cosmochimica Acta, 72, 1143–1153.

Mills, S.J., Christy, A.G., Génin, J.-M.R., Kameda, T., and Colombo, F. (2012) Nomenclature of the hydrotalcite supergroup: Natural layered double hydroxides. Mineralogical Magazine, 76, 1289–1336.

Monograph 255 (1967). U.S. National Bureau of Standards.

O'Loughlin, E.J., Kelly, S.D., Kemner, K.M., Csencsits, R., and Cook, R.E. (2003) Reduction of Ag(I), Au(III), Cu(II), and Hg(II) by Fe(II)/Fe(III) hydroxysulfate green rust. Chemosphere, 53, 437–446.

O'Loughlin, E.J., Larese-Casanova, P., Scherer, M., and Cook, R. (2007) Green rust formation from the bioreduction of γ –FeOOH (lepidocrocite): Comparison of several Shewanella species. Geomicrobiology Journal, 24, 211–230.

Ona-Nguema, G., Abdelmoula, M., Jorand, F., Benali, O., Géhin, A., Block, J.-C., and Génin, J.-M.R. (2002) Iron(II,III) hydroxycarbonate green rust formation and stabilization from lepidocrocite bioreduction. Environmental Science & Technology, 36, 16–20.

Ostwald, W. (1897) Studien ueber die Bildung und Umwandlung fester Koerper. Zeitschrift fuer Physikalische Chemie, 22, 289–330.

Parmar, N., and Beveridge, T.J. (2001) Formation of green rust and immobilization of nickel in response to bacterial reduction of hydrous ferric oxide. Geomicrobiology Journal, 18, 375–385.

Penn, R.L., Erbs, J., and Gulliver, D. (2006) Controlled growth of alpha-FeOOH nanorods by exploiting- oriented aggregation. Journal of Crystal Growth, 293, 1–4.

Raiswell, R. (2011) Iron transport from the continents to the open ocean: The aging-rejuvenation cycle. Elements, 7, 101–106.

Rennert, T., Eusterhues, K., De Andrade, V., and Totsche, K.U. (2012) Iron species in soils on a mofette site studied by Fe K-edge X-ray absorption near-edge spectroscopy. Chemical Geology, 332-333, 116–123.

Rousseau, M. (2011) Nacre, a natural biomaterial. In R. Pignatello, Ed., Biomaterials Applications for Nanomedicine pp. 281–298. InTech.

Ruby, C., Géhin, A., Abdelmoula, M., Génin, J.-M.R., and Jolivet, J.-P. (2003) Coprecipitation of Fe(II) and Fe(III) cations in sulphated aqueous medium and formation of hydroxysulphate green rust. Solid State Sciences, 5, 1055–1062.

Ruby, C., Aïssa, R., Géhin, A., Cortot, J., Abdelmoula, M., and Génin, J.-M. (2006) Green rusts synthesis by coprecipitation of FeII–FeIII ions and mass-balance diagram. Comptes Rendus Geoscience, 338, 420–432.

Scherrer, P. (1918) Bestimmung der Größe und der inneren Struktur von Kolloidteilchen mittels Röntgenstrahlen. Nachrichten von der Gesellschaft der Wissenschaften zu Göttingen, Mathematisch-Physikalische Klasse, 98–100.

Simon, L., François, M., Refait, P., Renaudin, G., Lelaurain, M., and Génin, J.-M.R. (2003) Structure of the Fe(II-III) layered double hydroxysulphate green rust two from Rietveld analysis. Solid State Sciences, 5, 327–334.

Skovbjerg, L.L., Stipp, S.L.S., Utsunomiya, S., and Ewing, R.C. (2006) The mechanisms of reduction of hexavalent chromium by green rust sodium sulphate: Formation of Cr-goethite. Geochimica et Cosmochimica Acta, 70, 3582–3592.

Stampfl, P.P. (1969) Ein basisches Eisen-II-III-Karbonat in Rost. Corrosion Science, 9, 185–187.

Sun, Z., Zhou, H., Glasby, G.P., Yang, Q., Yin, X., and Li, J. (2012) Mineralogical characterization and formation of Fe-Si oxyhydroxide deposits from modern seafloor hydrothermal vents. American Mineralogist, 98, 85–97.

Swedlund, P.J., Miskelly, G.M., and McQuillan, a. J. (2009) An attenuated total reflectance IR study of silicic acid adsorbed onto a ferric oxyhydroxide surface. Geochimica et Cosmochimica Acta, 73, 4199–4214.

Swietlik, J., Raczyk-Stanisławiak, U., Piszora, P., and Nawrocki, J. (2012) Corrosion in drinking water pipes: The importance of green rusts. Water Research, 46, 1–10.

Szytula, A., Burewicz, A., Dimitrijewic, Z., Krasnicki, S., Rzany, H., Todorovic, J., Wanic, A., and Wolski, W. (1968) Neutron diffraction studies of a-FeOOH. Physica Status Soliti, 26, 429–434.

Taylor, K.G., and Konhauser, K.O. (2011) Iron in Earth surface systems: A major player in chemical and biological processes. Elements, 7, 83–88.

Trolard, F., and Bourrié, G. (2012) Fougerite a natural layered double hydroxide in gley soil: habitus, structure, and some properties. In M. Valaskova and G.S. Martynkova, Eds., Clay Minerals in Nature - Their Characterization, Modification, and Application pp. 171–188. InTech.

Trolard, F., Genin, J.-M., Abdelmoula, M., Bourrie, G., Humbert, B., and Herbillion, A. (1997) Identification of a green rust mineral in a reductomorphic soil by Moessbauer and Raman spectroscopies. Geochimica et Cosmochimica Acta, 61, 1107–1111.

Trolard, F., Bourrié, G., Abdelmoula, M., Refait, P., and Feder, F. (2007) Fougerite, a new mineral of the pyroaurite-iowaite group: Description and crystal structure. Clays and Clay Minerals, 55, 323–334.

Usman, M., Hanna, K., Abdelmoula, M., Zegeye, a., Faure, P., and Ruby, C. (2012) Formation of green rust via mineralogical transformation of ferric oxides (ferrihydrite, goethite and hematite). Applied Clay Science, 64, 38–43.

Vargas, R., Louer, D., and Langford, J.I. (1983) Diffraction line profiles and scherrer constants for materials with hexagonal crystallites. Journal of Applied Crystallography, 16, 512–518.

Vignati, D.A.L., Ferrari, B.J.D., and Dominik, J. (2007) Laboratory-to-field extrapolation in aquatic sciences. Environmental Science & Technology, 41, 1067–1073.

Waychunas, G.A. (2001) Structure, aggregation and characterization of nanoparticles. In J.F. Banfield and A. Navrotsky, Eds., Reviews in Mineralogy and Geochemistry Vol. 44, pp. 105–166. Mineralogical Society of America and the Geochemical Society, Chantilly, Virginia.

Waychunas, G.A., Kim, C.S., and Banfield, J.F. (2005) Nanoparticulate iron oxide minerals in soils and sediments: unique properties and contaminant scavenging mechanisms. Journal of Nanoparticle Research, 7, 409–433.

Williams, A.G.B., and Scherer, M.M. (2001) Kinetics of Cr(VI) reduction by carbonate green rust. Environmental Science & Technology, 35, 3488–3494.

Xue, X., Penn, R.L., Leite, E.R., Huang, F., and Lin, Z. (2014) Crystal growth by oriented attachment: Kinetic models and control factors. CrystEngComm, 16, 1419–1429.

Zegeye, A., Bonneville, S., Benning, L.G., Sturm, A., Fowle, D.A., Jones, C., Canfield, D.E., Ruby, C., MacLean, L.C., Nomosatryo, S., and others (2012) Green rust formation controls nutrient availability in a ferruginous water column. Geology, 40, 599–602.

Zouboulis, A.I., and Moussas, P.A. (2008) Polyferric silicate sulphate (PFSiS): Preparation, characterisation and coagulation behaviour. Desalination, 224, 307–316.

FIGURE CAPTIONS

Figure 1. Pseudo-hexagonal natural green rust platelet from mine drainage outflow water. (a) TEM image of an aggregate of platelets, (b) HR-TEM image showing dark and light patches, with an inset of the FFT pattern showing the two stacked particles slightly rotated crystallographically with respect to each other, (c) results from comparing the STEM EDS (1 nm spot size) analyses of two dark and two light patches (EDS data not shown).

Figure 2. A different pseudo-hexagonal natural green rust platelet from mine outflow water. (a) TEM image of an aggregate of platelets; (b) bright field image of the inset in (a); (c) inverted and indexed SAED pattern of the same approximate area, with the spots used for DF imaging circled and labeled; (d)-(f) DF images of the same area as (b); (g) HR image with inset of whole-image FFT and the white box indicating the area for smaller-area FFT (h) and enlarged HR image (i); (j) HR image with white box indicating the area for (k) and (l); (m) EDS spectrum. Note that the strongest reflections in the FFTs in (h) and (l) are different.

Figure 3. Pseudo-hexagonal natural green rust platelet from mine drainage terrace sediment. (a) TEM image of a platelet; (b) bright field image of the inset in (a); (c) inverted and indexed SAED pattern of the same approximate area, with the spots used for DF imaging circled and labeled; (d)-(f) DF images of the same area as (b); (g) HR image showing mosaic of lattice fringes and amorphous patches; (h) enlarged area of (g) showing the fringes more clearly; (i) FFT of (g) showing faint spots matching the SAED pattern with one set of additional spots; (j) EDS spectrum of whole platelet, with inset showing trace Ni and Cu.

908 **Figure 4.** XRD spectra of syntheses (with number of days allowed to age) that produced
909 primarily sulfate green rust II (GR) (Simon et al. 2003) and other minor phases (M = magnetite).
910 Green rust and magnetite peaks are labeled with their crystallographic hkl plane(s).
911
912 **Figure 5.** Pseudo-hexagonal platelet synthesized in GR-A and sampled immediately upon
913 reaching pH 8. (a) TEM image of a platelet in an aggregate, (b) bright field image of the inset in
914 (a), (c) inverted and indexed SAED pattern of the same approximate area, with the spots used for
915 DF imaging circled and labeled, (d)-(f) DF images of the same area as (b), (g) and (h) HR images
916 showing lattice fringes, (i) FFT of (g) showing a clear hexagonal spot pattern, (j) EDS spectrum.
917 Arrows in (c) indicate an artifact ring (lines, not spots) from contamination on the C2 aperture.
918
919 **Figure 6.** Pseudo-hexagonal green rust platelets from synthesis GR-B, aged 54 days. (a) TEM
920 image of part of a platelet with nanoparticle aggregates on the surface; (b) medium magnification
921 showing dendritic areas of crystallinity more clearly; (c) inverted and indexed SAED pattern of
922 the approximate area imaged in (a), with the spots used for DF imaging circled and labeled; (d)
923 bright field image of the inset area in (a) and the same area used for DF imaging (e and f); (g)
924 HR-TEM of the area in (b); (h) zoomed-in area of (g) to better show faint lattice fringes; (i) FFT
925 of whole HR-TEM image in (g); (j) EDS spectrum of another area, shown in the inset; (k) a third
926 area showing different platelet shapes; (l) inverted SAED pattern of the circled area in (k); (m)
927 SEM image of (k) to show raised rims and interesting particle shape. Arrows in (c) and (i)
928 indicate an artifact ring (lines, not spots) from contamination on the C2 aperture.
929

Figure 7. GR-B dendrite patterns shown in Figure 6g, with small-area FFTs along the crystalline dendrites. (a) Modified image highlighting one dendritic pattern (dark area) by placing a semi-transparent white background over the areas not associated with this dendrite. The inset is the FFT of the whole image with the predominant pair of reflections is circled in white. (b) Map of FFT patterns on that same image, where each FFT only displays one or two pairs of the hexagonal pattern, some rotated slightly with respect to each other. FFT patterns along the same dendrite tend to match and align well.

Figure 8. Nanorods of green rust produced in synthesis GR-D. (a) TEM image of an aggregate of nanorods with vertically-aligned rods visible as diamond shapes (circled in white); (b) HR-TEM image of a single nanorod, with possible twin interfaces indicated by the black dashed lines; (c) FFT of the area outlined in white in (b); (d) nano-rod on end exhibiting large lattice fringes; (e) FFT of area outlined in white in (d); (f) simulated diffraction pattern of sulfate green rust II (Simon et al. 2003) oriented along the $\bar{1}00$ zone axis exactly matches the FFT pattern.

Figure 9. A comparison of the relative orientation of crystallites (0°, ~4° and >4° tilted) and how this affects the appearance of the SAED patterns and dark field images. The crystallites are represented here by spheres and circles, with lines indicating lattice fringes. A SAED pattern showing plane reflections of equal intensity would imply an untilted crystallite, and a dark field image of that crystallite created using the reflection indicated by the black circle would appear bright. Crystallites tilted ~4° exhibit SAED patterns with some reflections having reduced intensity (without showing new reflections), as well as reduced intensity for the dark field image.

952 SAED patterns of crystallites tilted greater than 4-10° will be missing some reflections
953 completely, and the dark field image will appear dark.
954
955
956
957
958

TABLES

Table 1. Synthesis conditions where sulfate green rust II was formed according to XRD.

Synth. name	$[Fe^{II}]$ (M)	$[Fe^{III}]^a$ (M)	nFe^{II}/nFe^{III}	$[Fe_{total}]$ (M)	nFe^{III}/nFe_{total}	Fe_{soln} (L)	nOH^-/nFe_{total}	$[OH^-]$ (M)	OH^- added (L)	Anoxic?	Dumped or titrated OH^-?
GR-A	0.134	0.062	2.15	0.196	0.32	0.1	2.04	0.80	0.05	Yes	titrated
GR-B	0.144	0.055	2.63	0.199	0.28	0.1	2.01	0.40	0.10	No	dumped
GR-C	0.144	0.055	2.60	0.199	0.28	0.1	2.06	0.41	0.10	Yes	dumped
GR-D	0.075	0.082	0.91	0.160	0.48	0.1	1.03	0.41	0.04	Yes	titrated

Note: Concentrations are in moles per liter (M), ratios are molar (n) ratios.
[a] $Fe_2(SO_4)_3 \bullet nH_2O$ reagents used: 97%, "pentahydrate," Acros Organics (GR-A); puriss p.a., 21-23% Fe basis, Sigma-Aldrich (GR-B, C); GR grade, EM Science (GR-D).

Table 2. D-spacings (in Å) for pseudo-hexagonal platelets found in outflow water and terrace sediment.

Reference Data[a]					Outflow water		Terrace Sediment	
					i.e. Figures 1-2		i.e. Figure 3	
GR-SO4		GR-Na,SO4		hematite	SAED	FFT	SAED	FFT
d	hkl	d	hkl	d	d	d	d	d
11.01	001	10.98	001					
		7.37						
5.51	002	5.49	002					
4.78	100	4.78	110					
					4.45			
4.39	101	4.38	111					
		3.91	021					
					3.86			
3.67	003	3.66	003	3.68	3.73			
					3.55			
					3.37-3.41			
2.91	103	3.07	120				2.94	
2.76, 2.75	110,004	2.75	030,004					
2.68	-1-11	2.67	031	2.69				
		2.60	014		2.57-2.62			
2.47	-1-12	2.46	032	2.51	2.45-2.52	2.54	2.49	2.52-2.61
2.34,2.39	201,200							
2.21	-1-13,005	2.20	033,005	2.20			2.22	
2.00	105,203				2.29			
1.95	-1-14	1.94	034		1.92			
1.81,1.84	210,006	1.80,1.83	140,006	1.84				
1.72	-1-15	1.72	035	1.69				
1.60,1.62	300,213	1.59	330	1.60			1.61	
1.58	301	1.57	331,007					
1.53	302	1.53	332		1.54			1.51
1.49	107	1.49	117	1.49	1.48-1.5		1.48	
1.46	303	1.46	333	1.45	1.43	1.46	1.46	
		1.37	060,334					
		1.36	061	1.35				
		1.33	062		1.28			
		1.29	063,335				1.25	

Note: Figure numbers are given for reference, but the d-spacing values (in Å) are representative of multiple areas. Grey highlighted cells represent the values that appear in a hexagonal pattern when the crystal is oriented along the [001] zone axis.

[a]Reference data sources: GR-SO_4 (Simon et al. 2003), GR-Na,SO_4 (Christiansen et al. 2009), hematite (ICDD PDF card 00-001-1053 (Hanawalt et al. 1938))

{Note to typesetter: all minus signs are overbars}

Table 3. D-spacing data (in Å) for synthetic green rust materials, from XRD, SAED and FFT. D-spacings are divided based on whether they were from sharp spots (nanoparticles) or broad spots (platelets). Grey highlighted cells represent the values that appear in a hexagonal pattern when the crystal is oriented along the [001] zone axis.

Reference Data[a]				GR-A pH8 + 2 days[b]				GR-B + 54 days			
				i.e. Figure 5				i.e. Figure 6			
GR-Na,SO4		goethite	magnetite	XRD	SAED	SAED	FFT	XRD	SAED	SAED	FFT
d	hkl	d	d	d	d (np's)	d (platelets)		d	d (np's)	d (platelets)	
10.98	001			11.32				11.07			
7.37									7.52		
5.49	002	4.98		5.57				5.50			
4.78	110		4.85						4.78		
				4.68							
4.38	111			4.30							
		4.19									
3.91	021										
3.66	003			3.69				3.66			
				3.51							
							3.32[c]				
3.07	120		2.97					2.96	2.94		3.03
2.75	030,004			2.76				2.75			
2.67	031	2.69		2.69				2.68			
2.60	014		2.53	2.55		2.53	2.54-2.57	2.53	2.50	2.55	2.54-2.57
2.46	032	2.45,2.49		2.47				2.46			
			2.42						2.39		
2.20	033,005	2.19		2.21,2.24	2.21			2.20			
			2.10	2.00,2.04				2.08	2.08		
1.94	034			1.95	1.93			1.94	1.91	1.87	
1.80, 1.83	140, 006			1.83				1.81,1.83			
1.72	035		1.72	1.72	1.71			1.72	1.70		
1.59	330	1.66	1.62					1.61	1.59		
1.57	331,007	1.56		1.58				1.57			
1.53	332				1.53						
1.49	117		1.49			1.47				1.49	
1.46	333				1.44				1.46		
1.37	060,334		1.42								
1.36	061	1.36									
1.33	062								1.31		
1.29	063,335										

[a]Reference data sources: GR-Na,SO_4 (Christiansen et al. 2009), goethite (ICDD PDF card 01-074-2195 (Szytula et al. 1968)), magnetite (PDF card 00-019-0629 ("Monograph 255" 1967)).
[b]After sample reached pH 8, XRD data was from 2 days aged, while TEM data was taken from the fresh sample.
[c]Not a spot in the typical hexagonal pattern.

985 **Table 3. D-spacings table, continued.**
986

Reference Data[a]				GR-C + 2 days			GR-D		
				i.e. Figure 7			i.e. Figure 8		
GR-Na,SO4		goethite	magnetite	XRD	SAED	SAED	XRD	SAED	FFT
d	hkl	d	d	d	d (np's)	d (plate)	d	d (nanorods)	
10.98	001			11.05			11.16		10.0-10.4
7.37									
					6.02				
5.49	002	4.97		5.50			5.55		
4.78	110		4.85		4.81				4.70, 4.89
									4.53-4.63
4.38	111								
		4.17			4.15				
3.91	021								
								3.87	
3.66	003			3.66			3.69		
					3.54				
3.07	120		2.97	2.98	2.97		3.17		
2.75	030,004						2.77		
2.67	031	2.69		2.67			2.69	2.67	
2.60	014		2.53	2.53	2.53	2.53		2.51	2.54-2.57
2.46	032	2.45,2.49		2.46			2.48		
			2.42		2.41				2.35
2.20	033,005	2.19		2.20			2.21	2.19	2.20,2.25
			2.10	2.08	2.09				
1.94	034			1.95			1.96	1.88	
1.80,1.83	140,006			1.83	1.86				
1.72	035		1.72	1.71	1.71		1.72	1.69	
1.59	330	1.66	1.62	1.62	1.61		1.59		
1.57	331,007	1.56					1.58	1.57	
1.53	332						1.53		
1.49	117		1.49		1.48	1.47		1.48	
1.46	333							1.45	
1.37	060,334		1.42						
1.36	061	1.36							
1.33	062				1.31				
1.29	063,335								

987 [a]Reference data sources: GR-Na,SO_4 (Christiansen et al. 2009), goethite (ICDD PDF card 01-074-2195 (Szytula et
988 al. 1968)), magnetite (ICDD PDF card 00-019-0629 ("Monograph 255" 1967)).
989

990

991 **Table 4. Crystallite sizes calculated from XRD peak broadening and K = 1.**

GR-SO_4	**GR-A, 93d**		**GR-B, 64d**		**GR-C, 33d**		**GR-D, 0d**	
(h,k,l)	d (Å)	size (nm)	d (Å)	size (nm)	d (Å)	size (nm)	d (Å)	size (nm)
(001)	11.12	23	11.32	23	11.07	23	11.16	14
(002)	5.51	24	5.56	24	5.50	25	5.55	15
(101)	4.20	9						
(003)	3.66	26	3.69	26	3.66	27	3.69	14
			2.76	48	2.75	40	2.77	16
(111)	2.67	9	2.66	4	2.68	38	2.69	26
(112)	2.46	35	2.47	27	2.46	29	2.48	20
(005)	2.20	27	2.21	25	2.20	24	2.21	17
(114)	1.94	30	1.95	24	1.94	34	1.96	17
(006)	1.83	32	1.83	28	1.83	28		
					1.81	19		
(115)[a]	1.72	31	1.72	22	1.72	23	1.72	12
(205)[a]	1.62	37	1.62	17	1.61	21		
(300)	1.59	46					1.59	17
(007)	1.57	26			1.57	63	1.58	15
							1.53	28
All peaks								
Avg		24		25		28		17
Stdev		9		12		7		5
(001), (002), (003) peaks								
Avg		24		24		25		14
Stdev		1.7		1.6		1.9		0.7

992 Note: XRD spectra used were from aged (with aging time in days (d) indicated) samples. Only GR-SO_4 peaks are
993 shown (Simon et al. 2003). Averages (Avg) and standard deviations (Stdev) are also shown.
994 [a]Shares a peak position with magnetite

995

996

997

998 **Table 5. Fe/S atomic ratios for different natural and synthetic particles, as determined by**
999 **TEM-EDS.**

Sample	Fe/S	Particle type
Outflow water	14	platelets
Terrace sediment	59	platelets
GR-A	4	platelets
GR-B	7	platelets
	142	nanomagnetite
GR-C	8	platelets & nanomagnetite
GR-D	56	nanorods

1000

1001
1002

1003

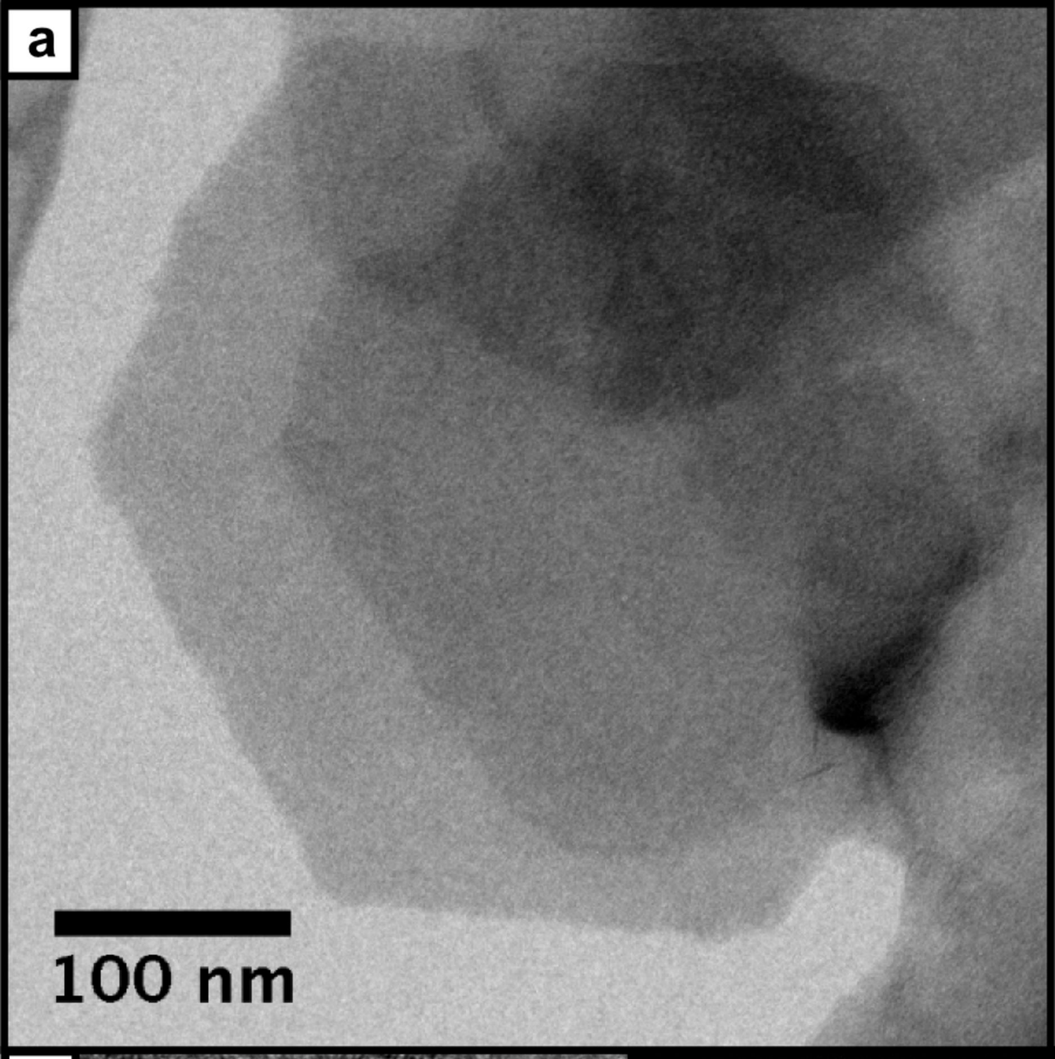

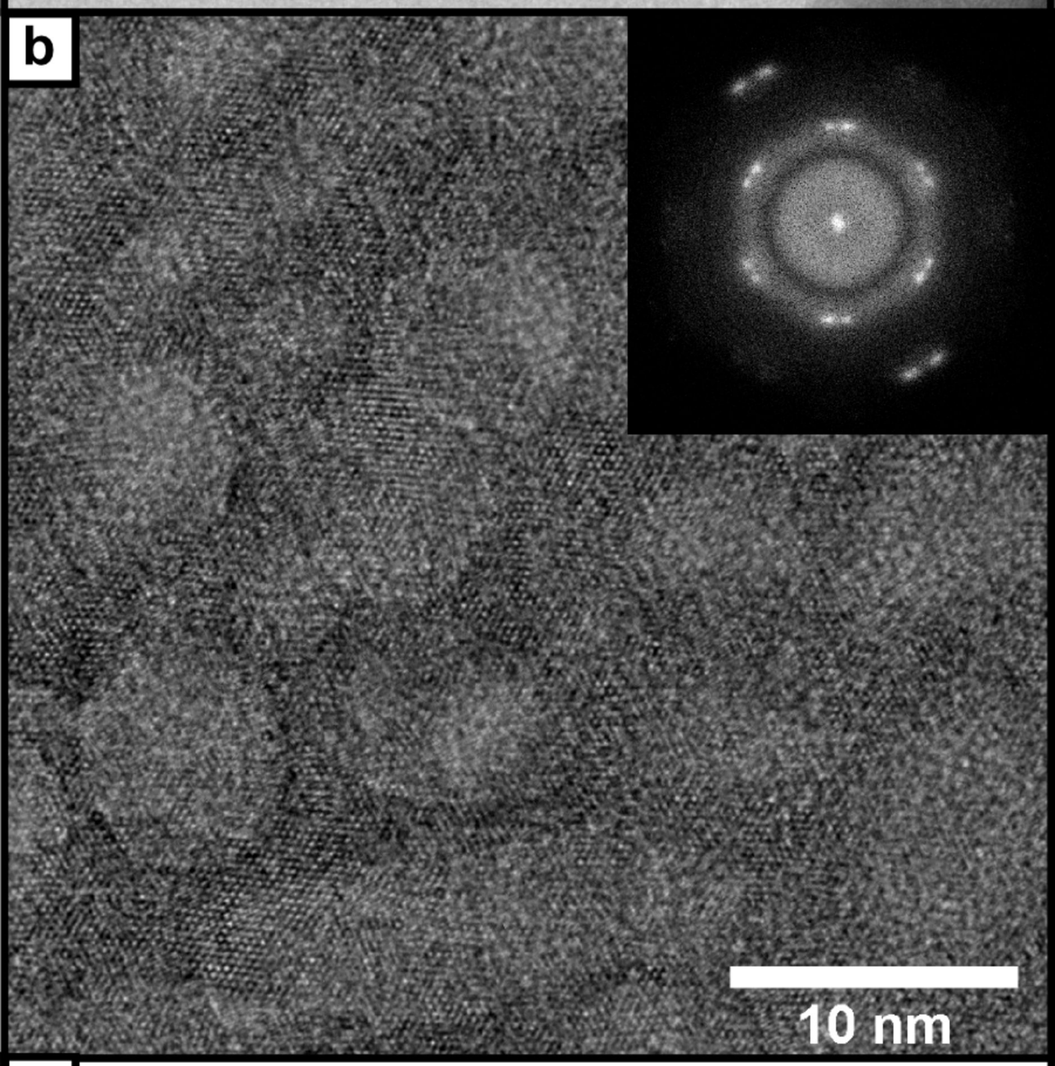

c

Dark patches	Light patches
crystalline	amorphous
lower Si/Fe	higher Si/Fe
(0.12, 0.19)	(0.44, 0.47)
Zn	no Zn
S	no S

Figure 1

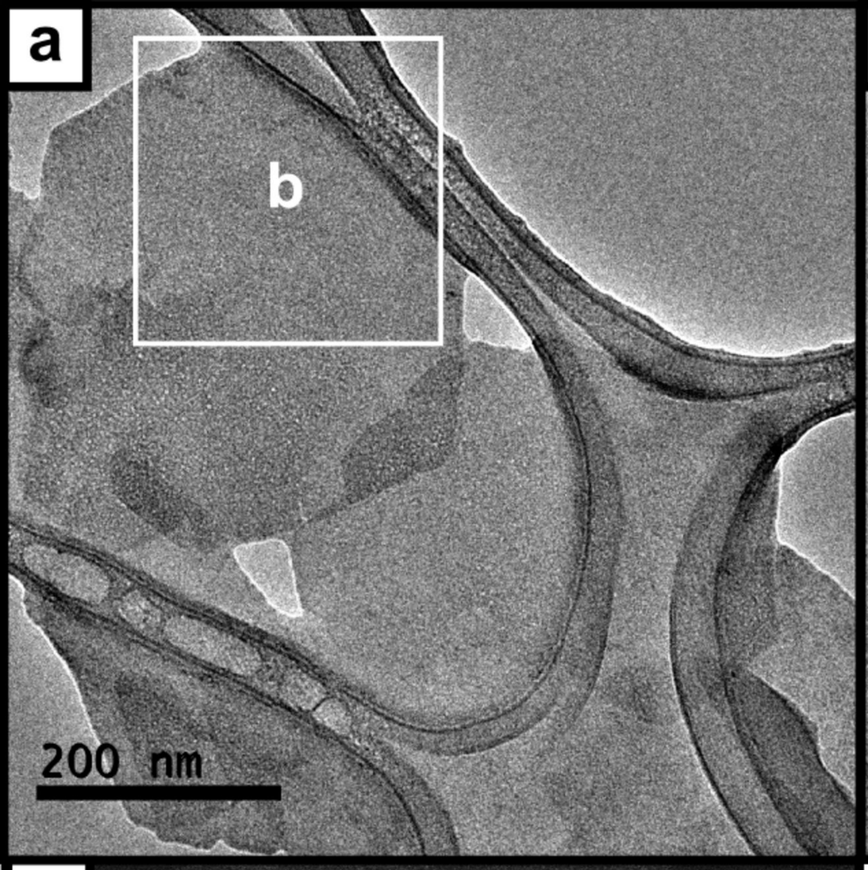
a
b
200 nm

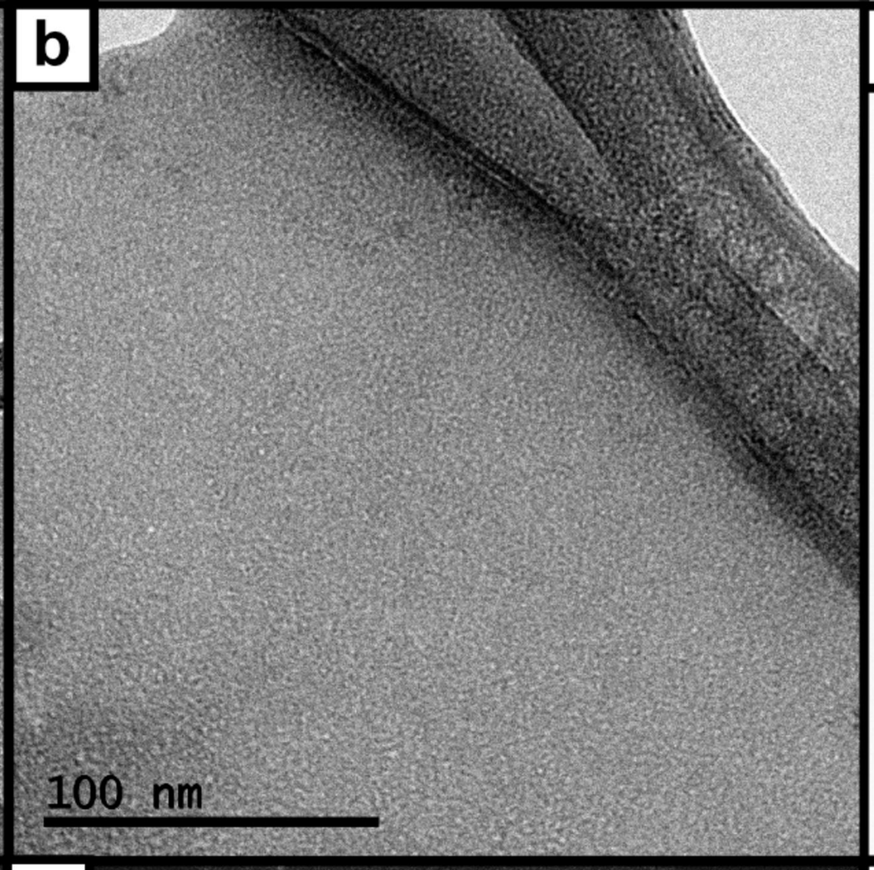
b
100 nm

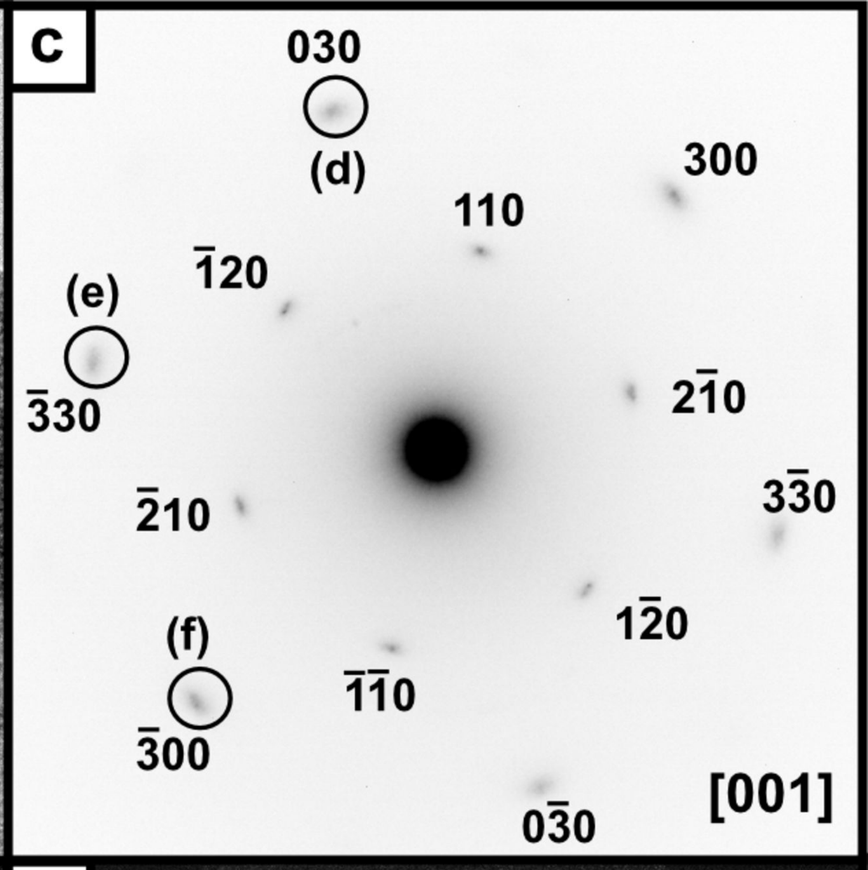
c
030
(d)
300
110
$\bar{1}20$
(e)
$\bar{3}30$
$2\bar{1}0$
$\bar{2}10$
$3\bar{3}0$
$1\bar{2}0$
(f)
$\bar{1}\bar{1}0$
$\bar{3}00$
$0\bar{3}0$
[001]

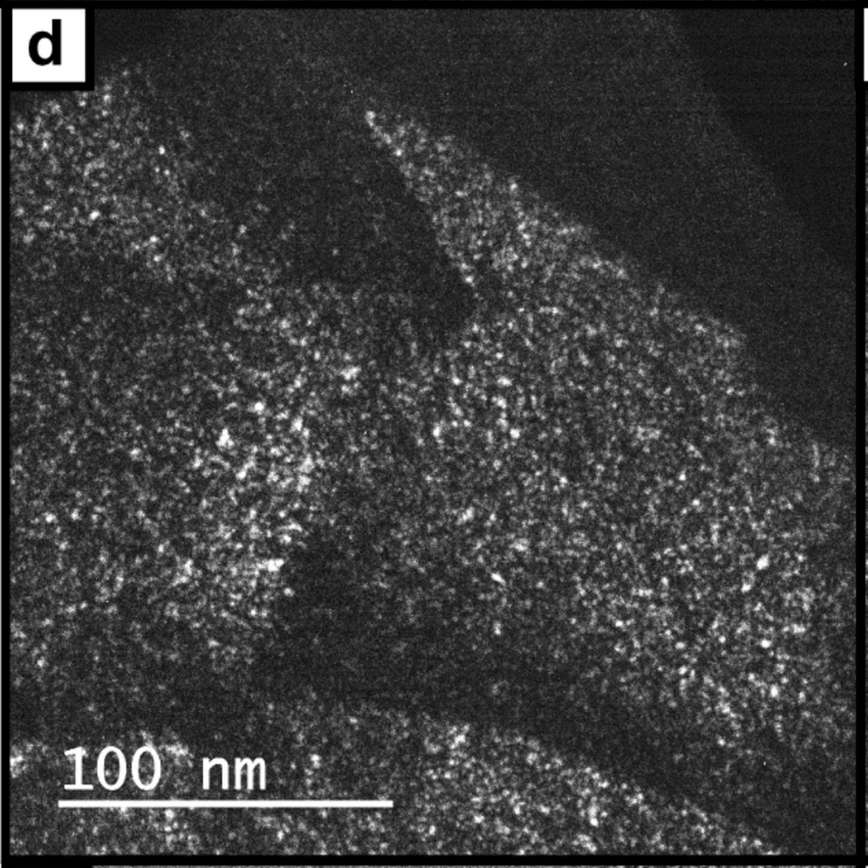
d
100 nm

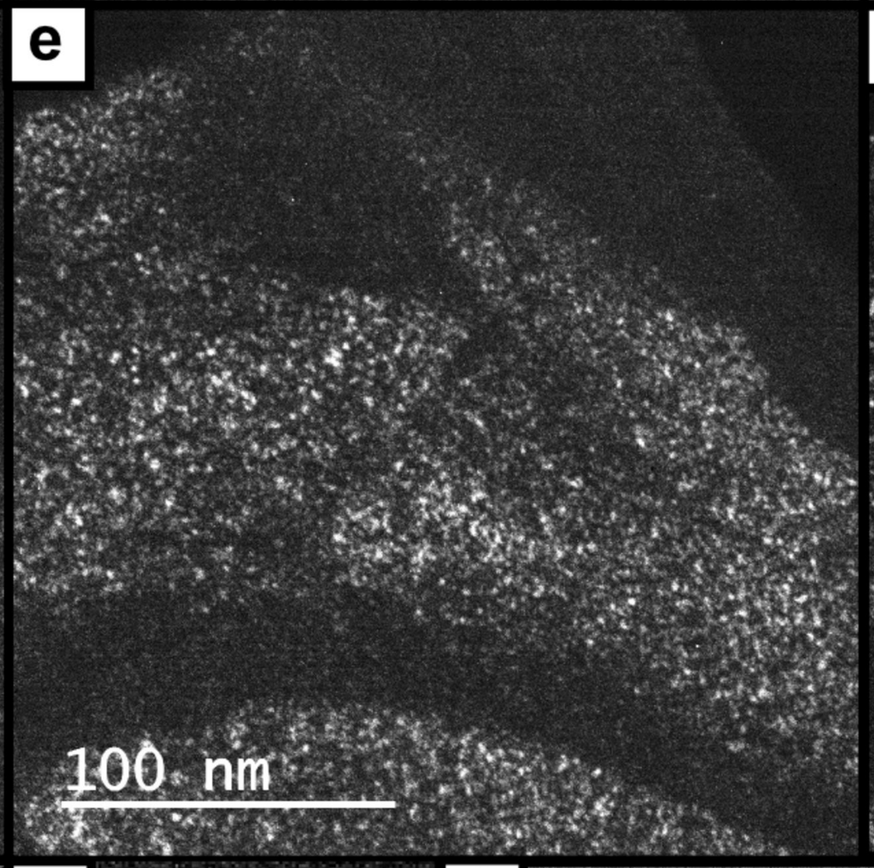
e
100 nm

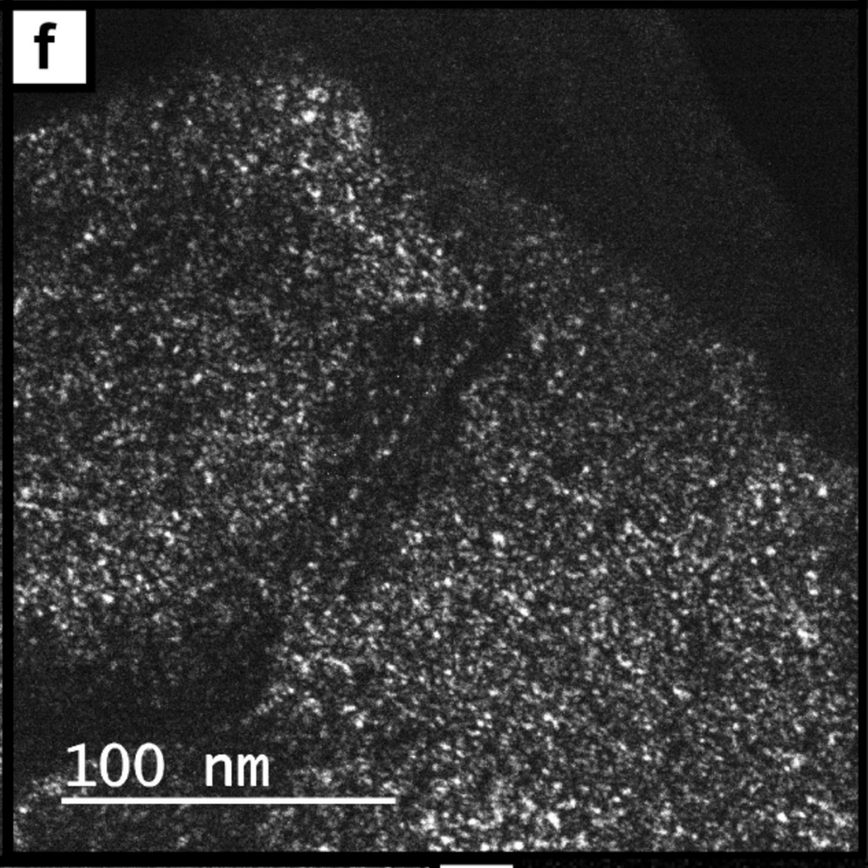
f
100 nm

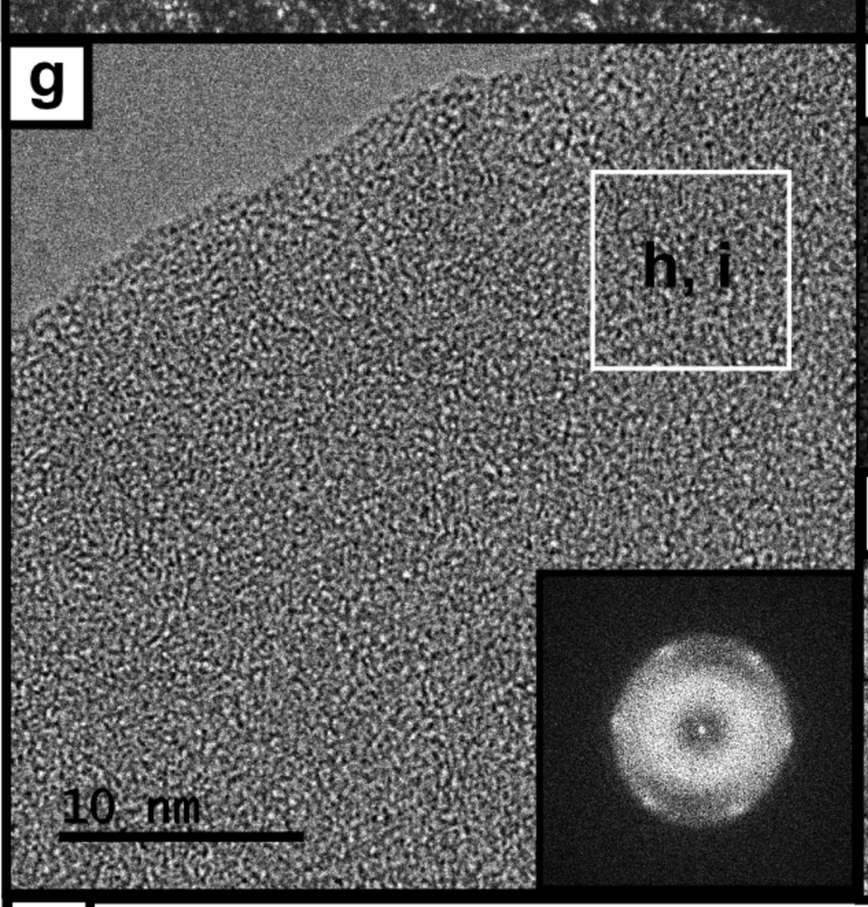
g
h, i
10 nm

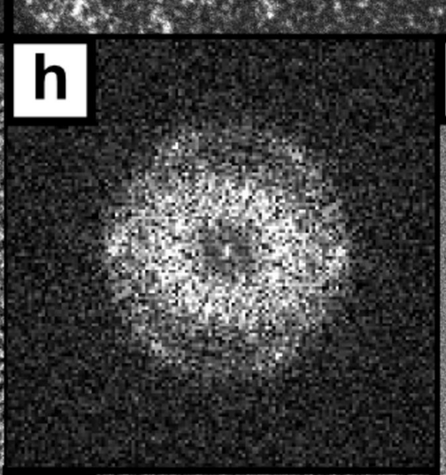
h

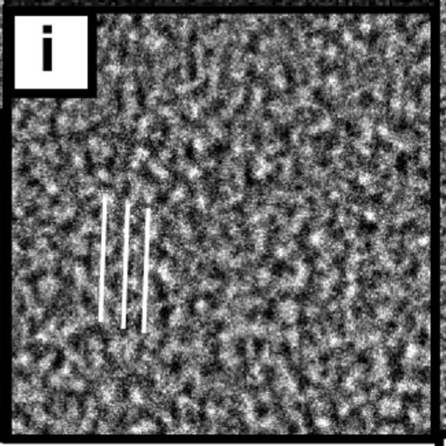
i

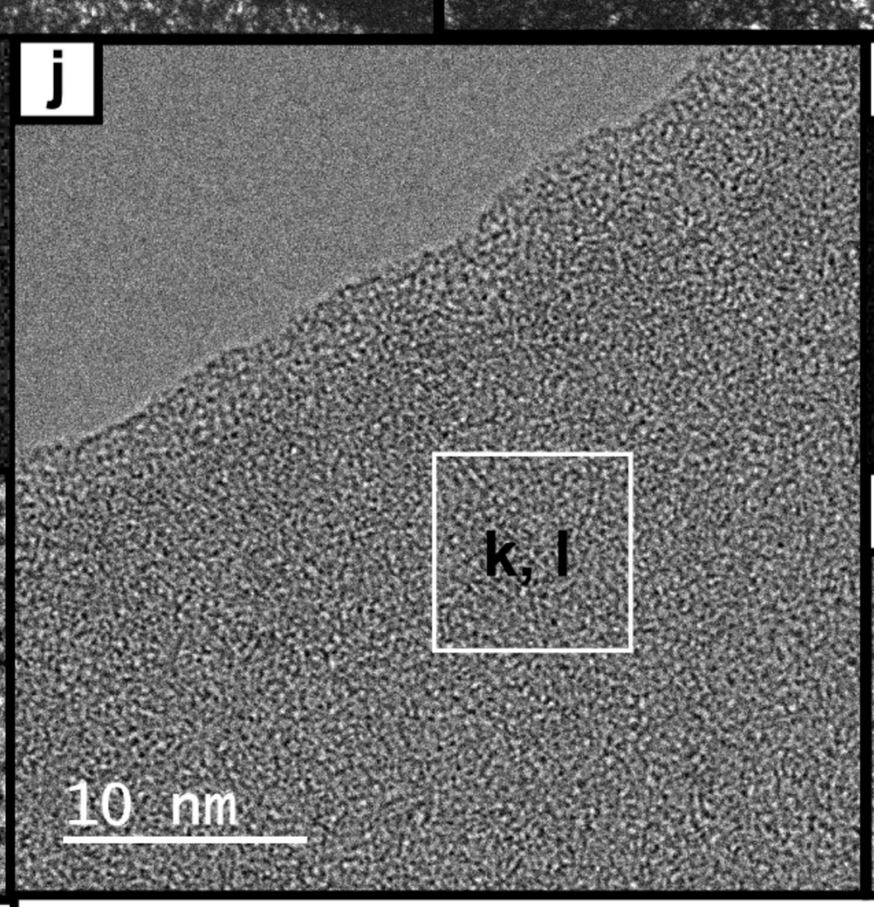
j
k, l
10 nm

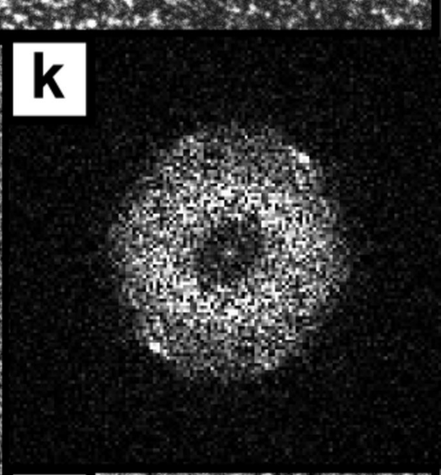
k

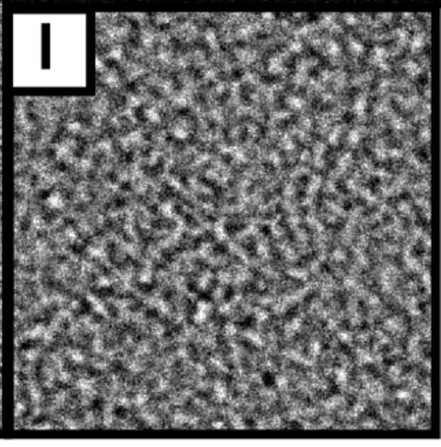
l

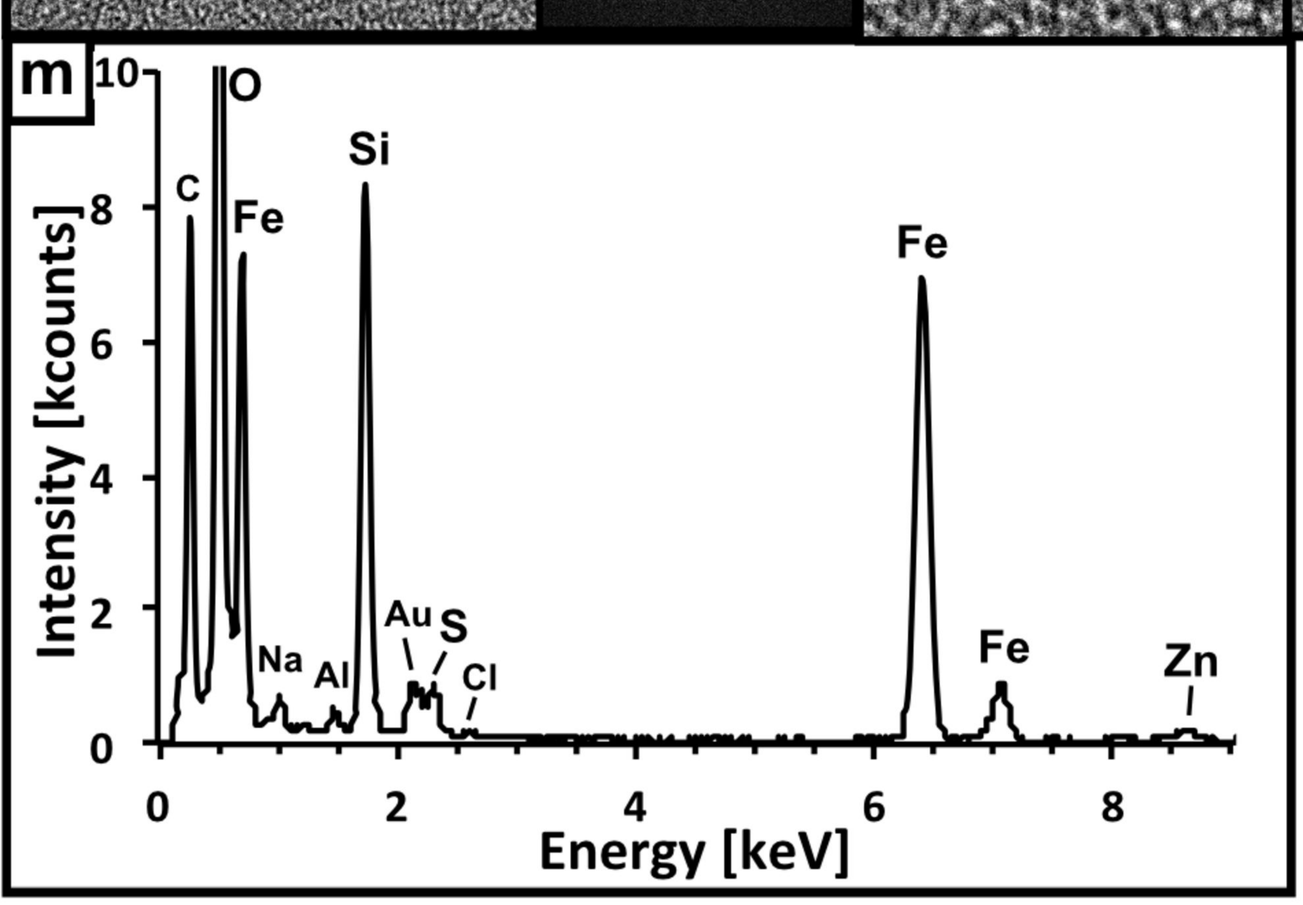
m
10
8
6
4
2
0
Intensity [kcounts]
C
O
Fe
Si
Na
Al
Au
S
Cl
Fe
Fe
Zn
0
2
4
6
8
Energy [keV]

Figure 2

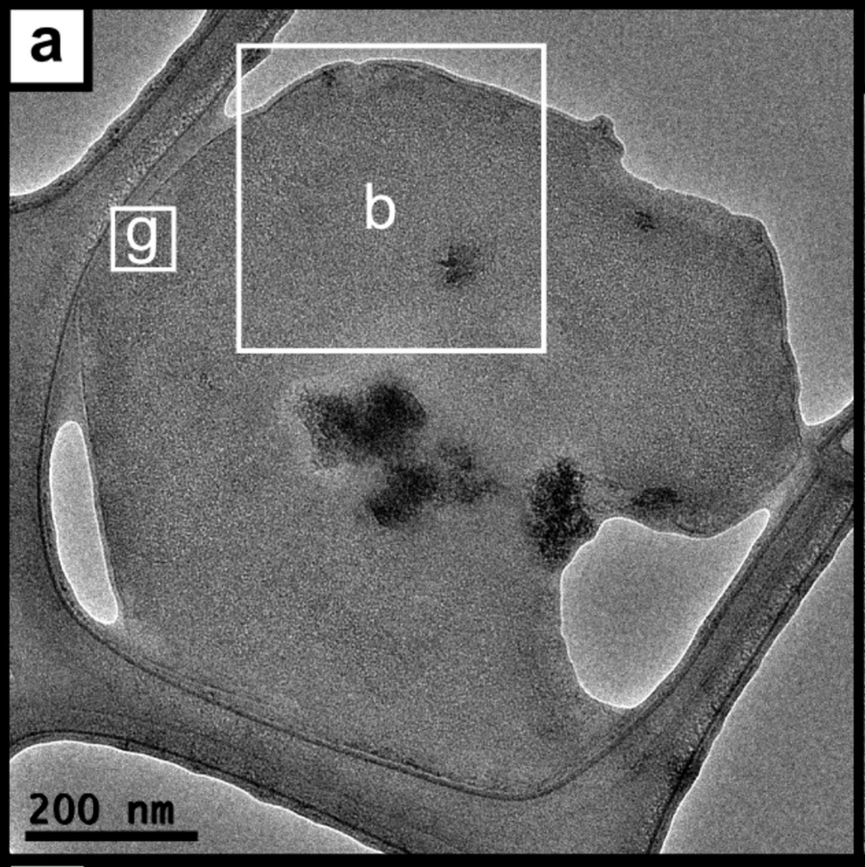
a
b
g
200 nm

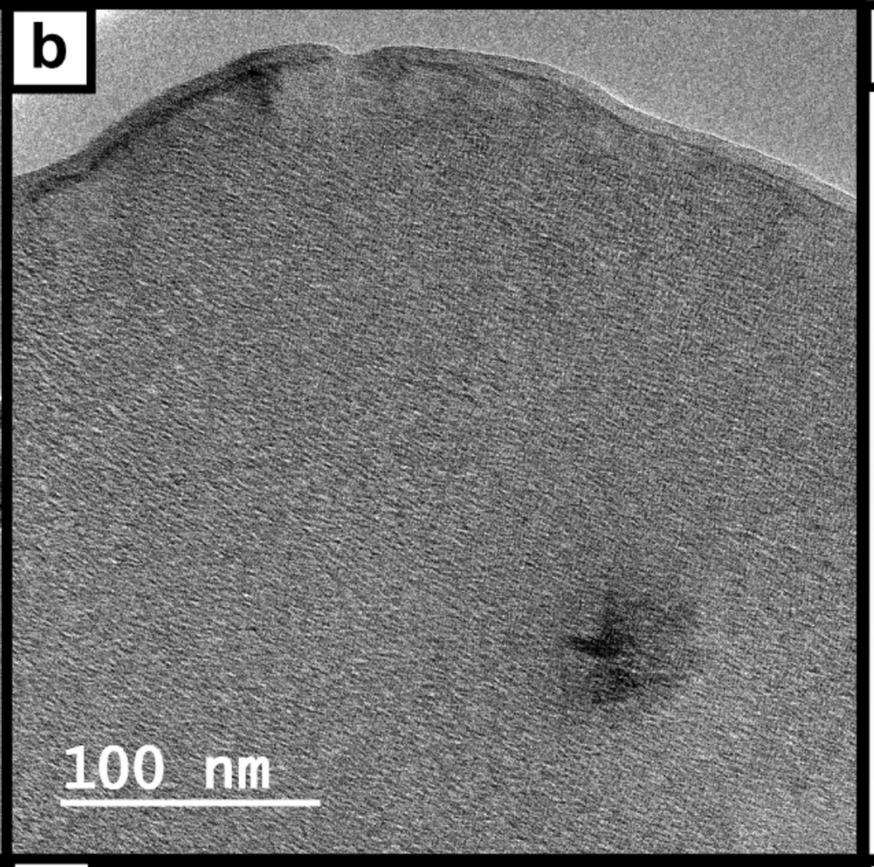
b
100 nm

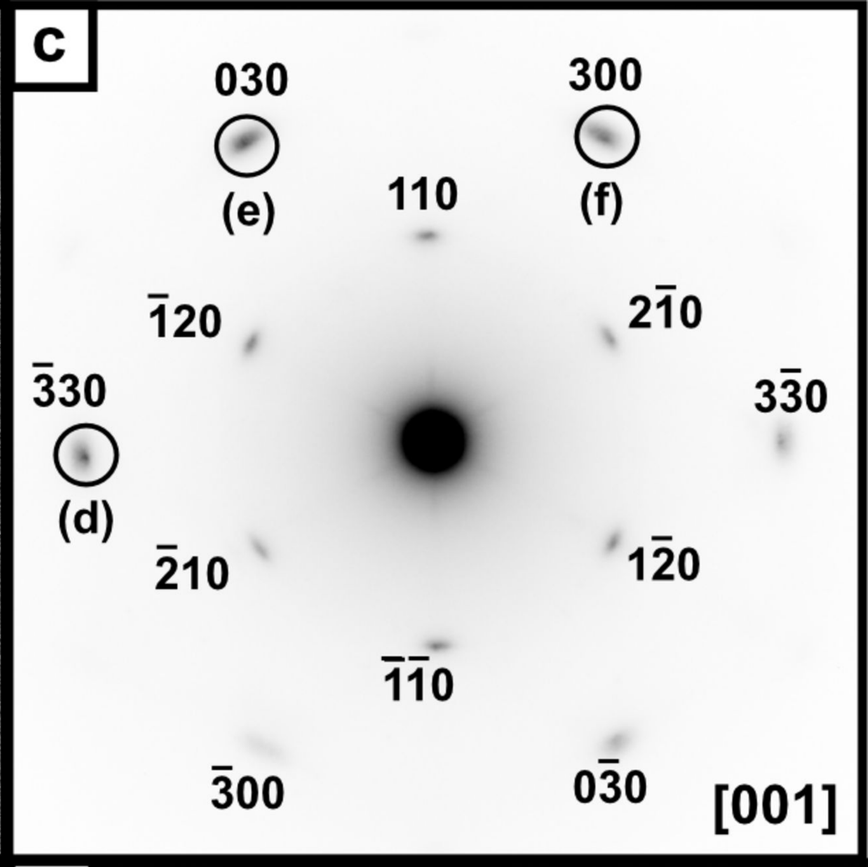
c
030
300
(e)
110
(f)
$\bar{1}20$
$2\bar{1}0$
$\bar{3}30$
$3\bar{3}0$
(d)
$\bar{2}10$
$1\bar{2}0$
$\bar{1}\bar{1}0$
$\bar{3}00$
$0\bar{3}0$
[001]

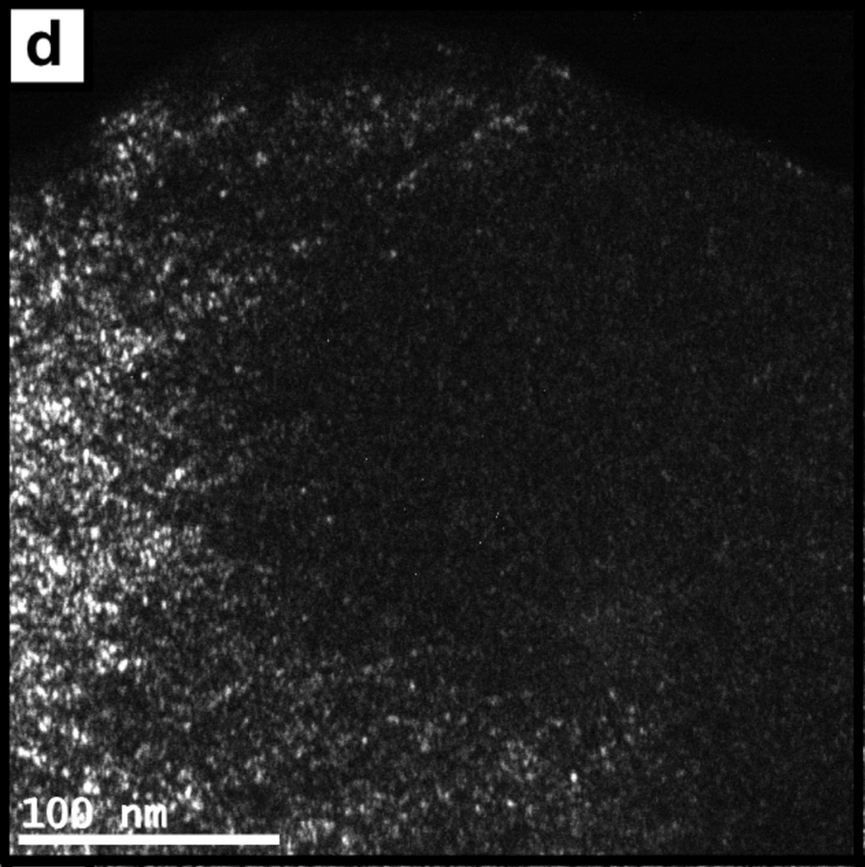
d
100 nm

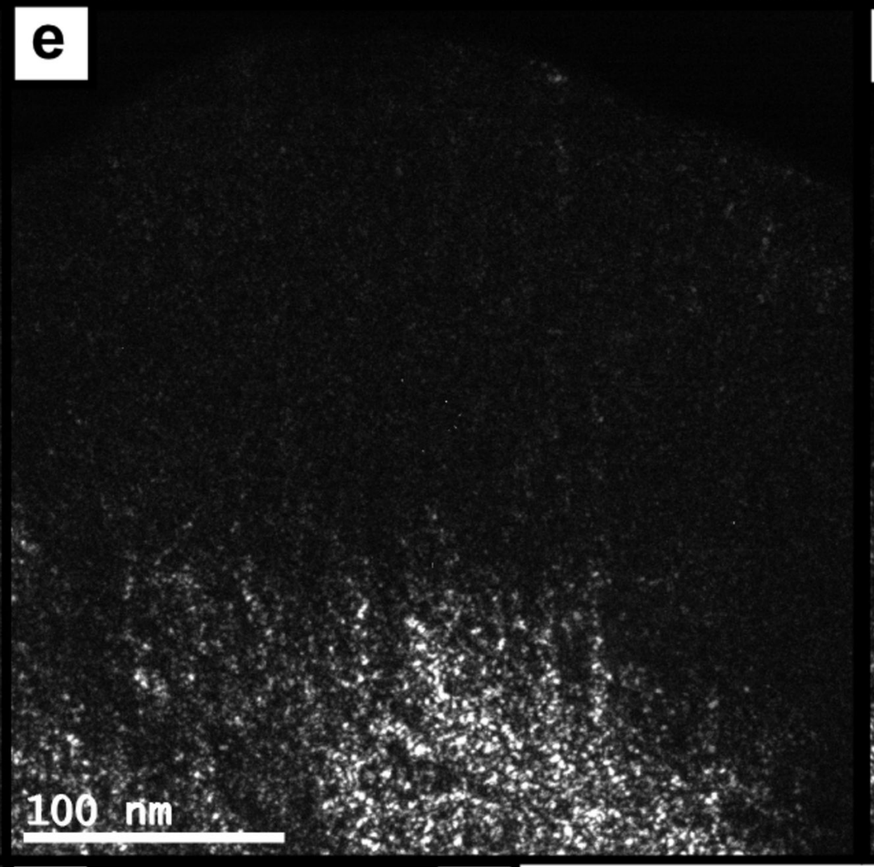
e
100 nm

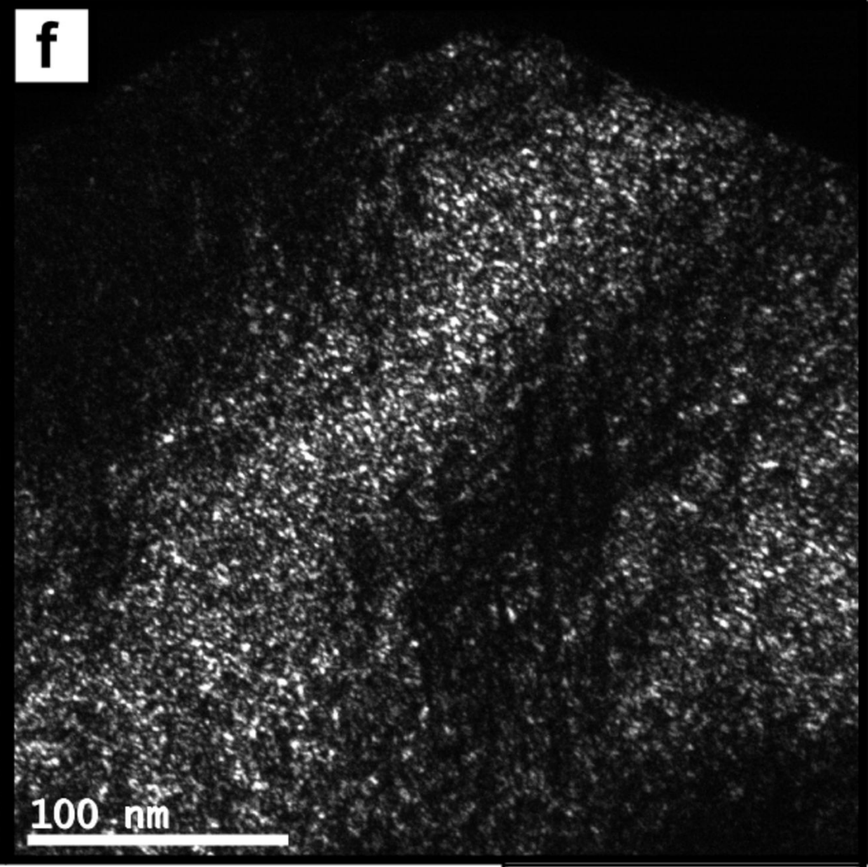
f
100 nm

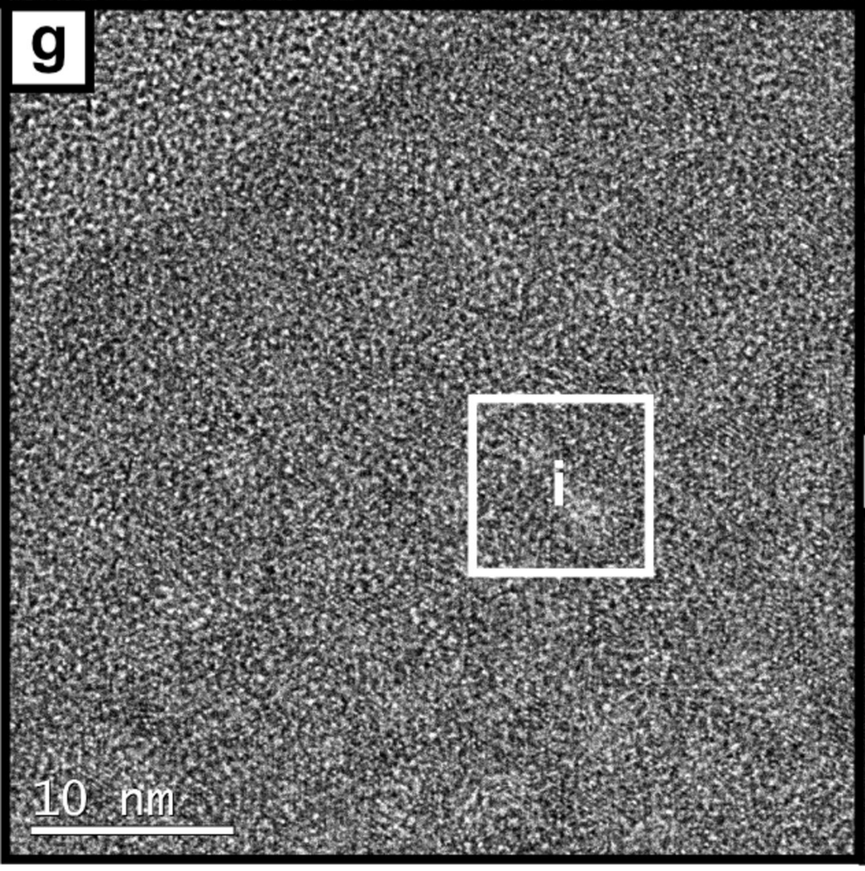
g
i
10 nm

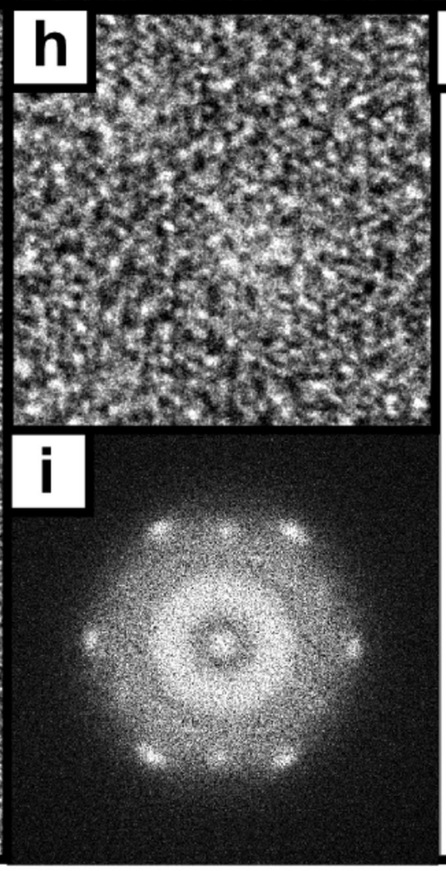
h
i

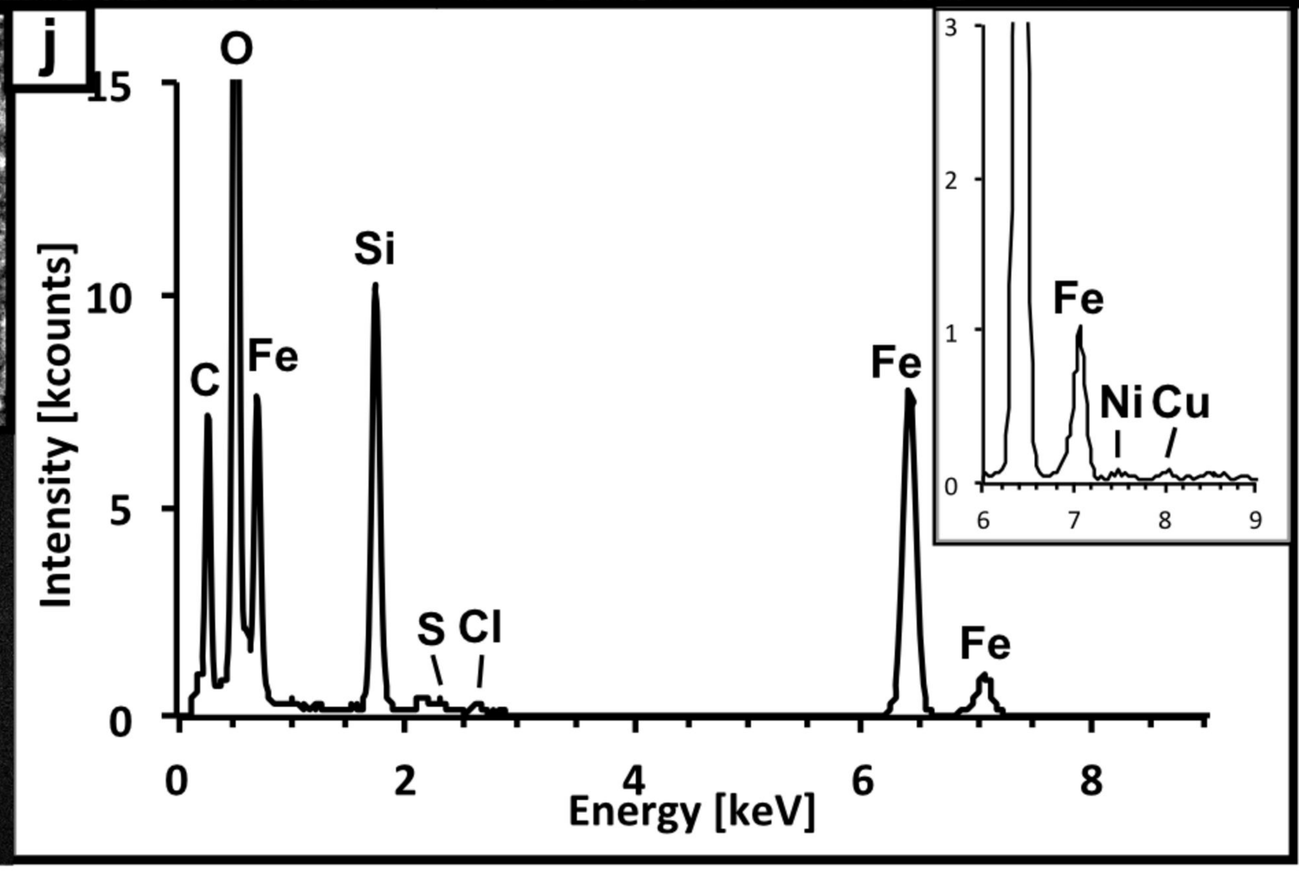
j
Intensity [kcounts]
Energy [keV]
O
C
Fe
Si
S
Cl
Fe
Fe
Ni
Cu

FIgure 3

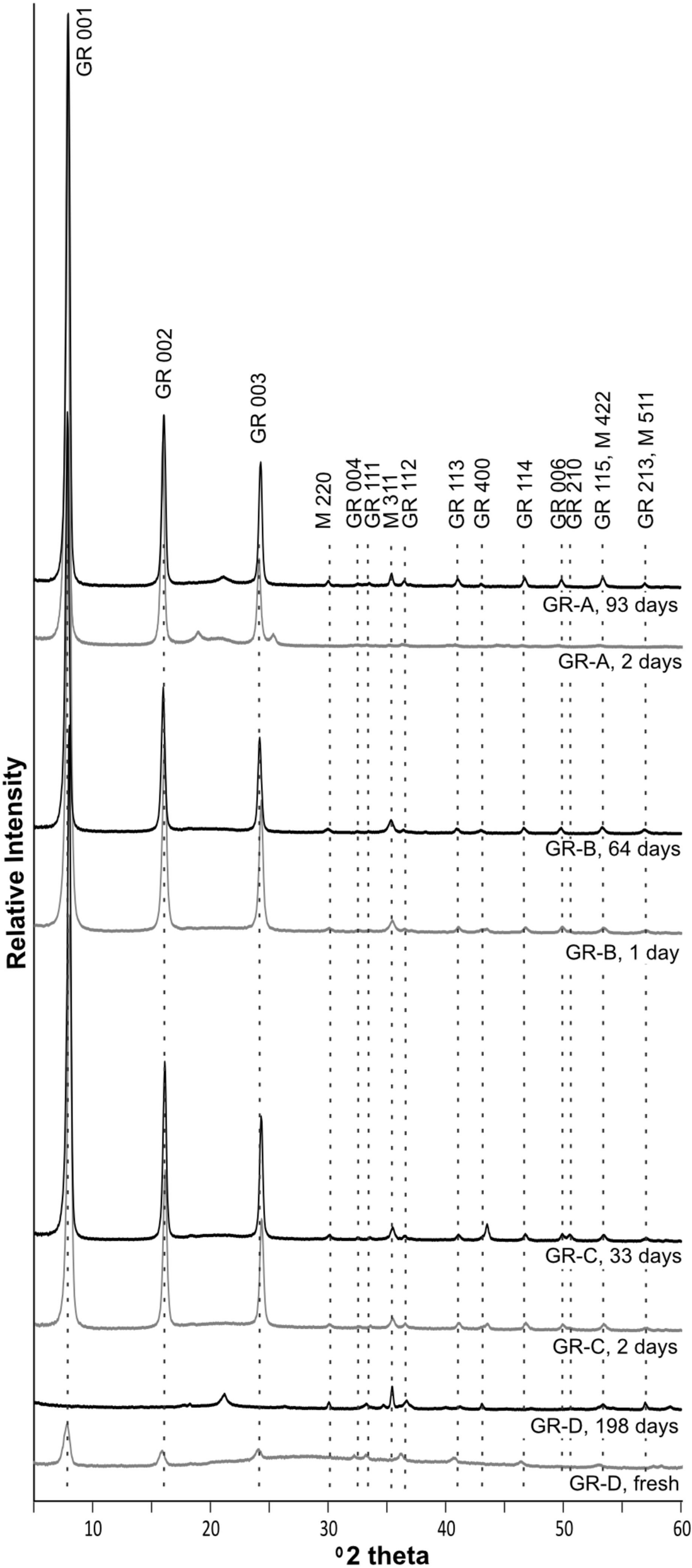
GR 001
GR 002
GR 003
M 220
GR 004
GR 111
M 311
GR 112
GR 113
GR 400
GR 114
GR 006
GR 210
GR 115, M 422
GR 213, M 511
GR-A, 93 days
GR-A, 2 days
GR-B, 64 days
GR-B, 1 day
GR-C, 33 days
GR-C, 2 days
GR-D, 198 days
GR-D, fresh
Relative Intensity
10
20
30
40
50
60
⁰2 theta

Figure 4

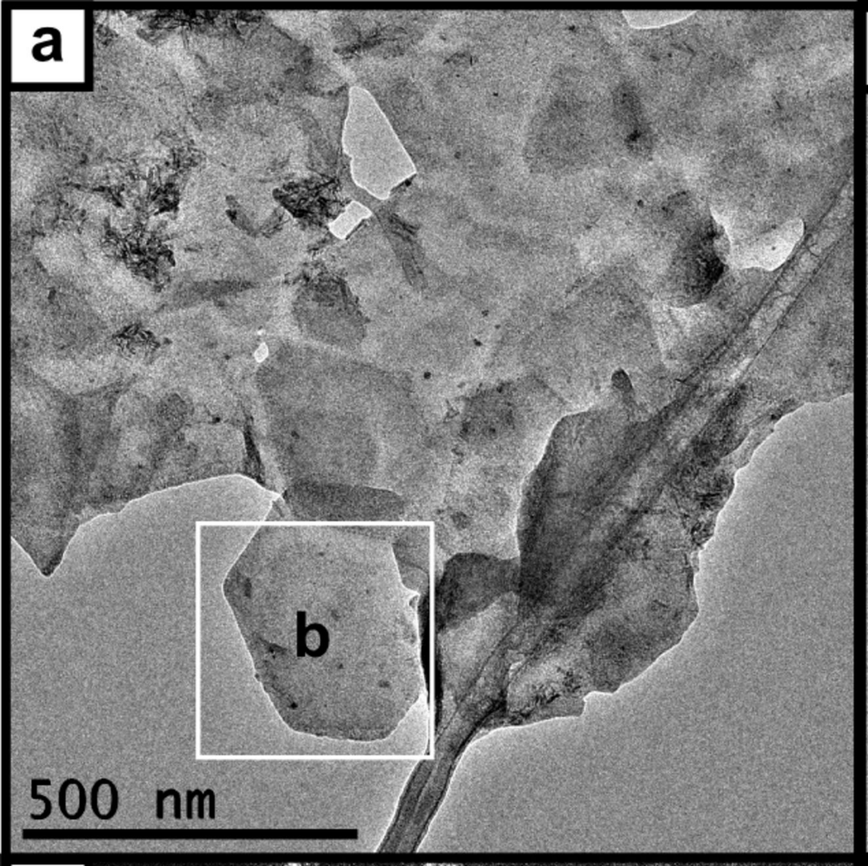
a
b
500 nm

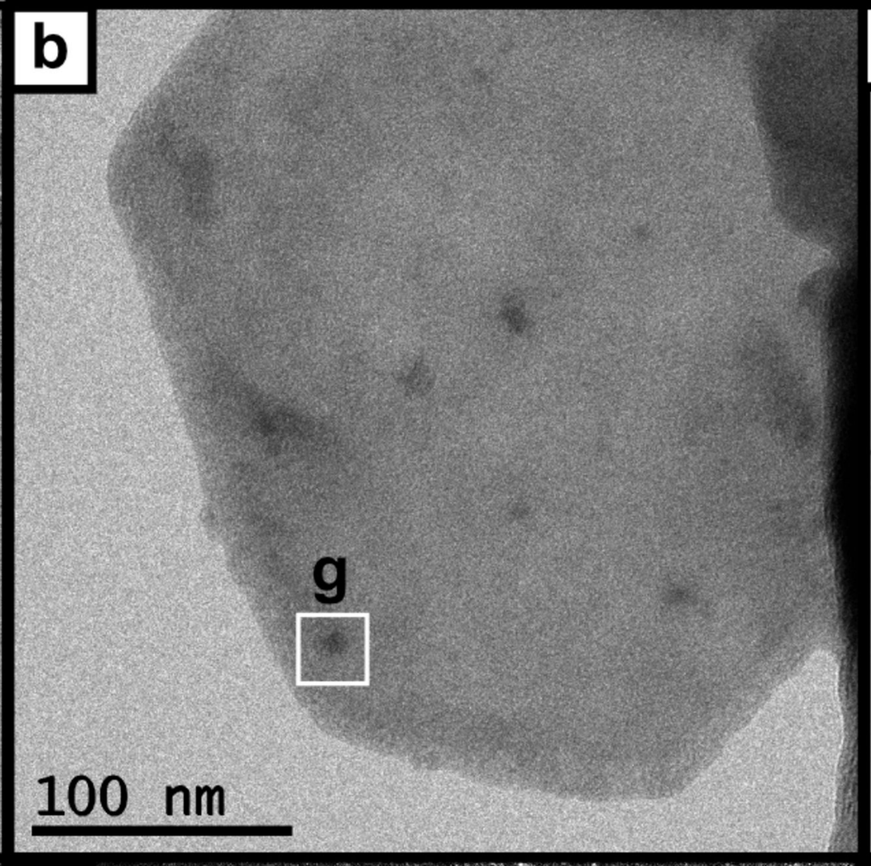
b
g
100 nm

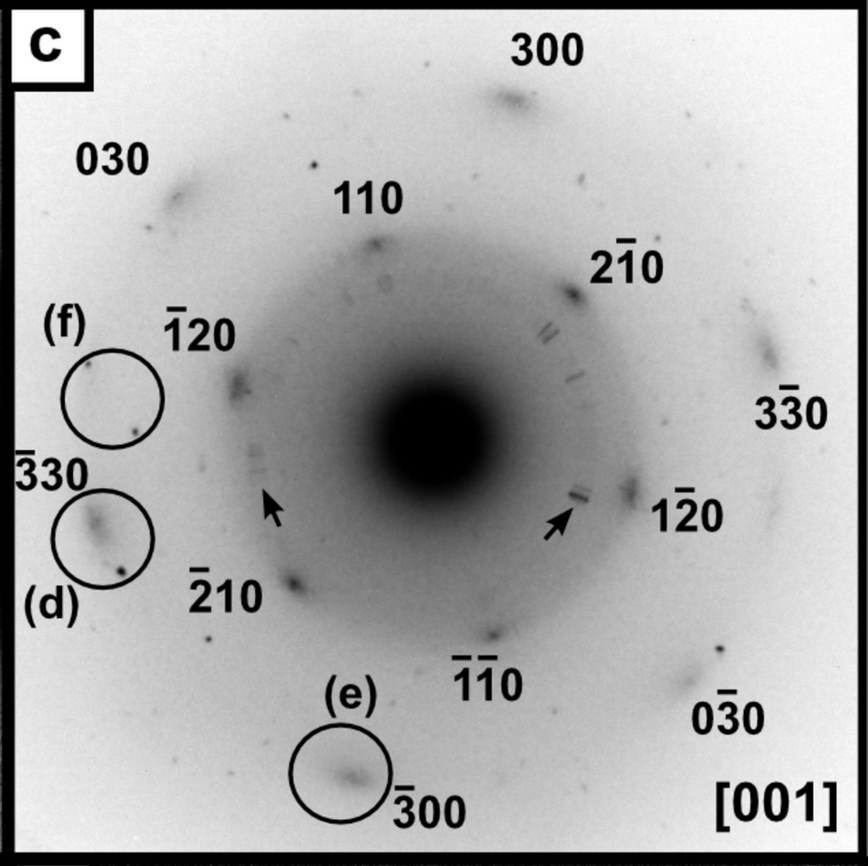
c
300
030
110
2$\bar{1}$0
(f)
$\bar{1}$20
3$\bar{3}$0
$\bar{3}$30
1$\bar{2}$0
(d)
$\bar{2}$10
$\bar{1}\bar{1}$0
(e)
0$\bar{3}$0
$\bar{3}$00
[001]

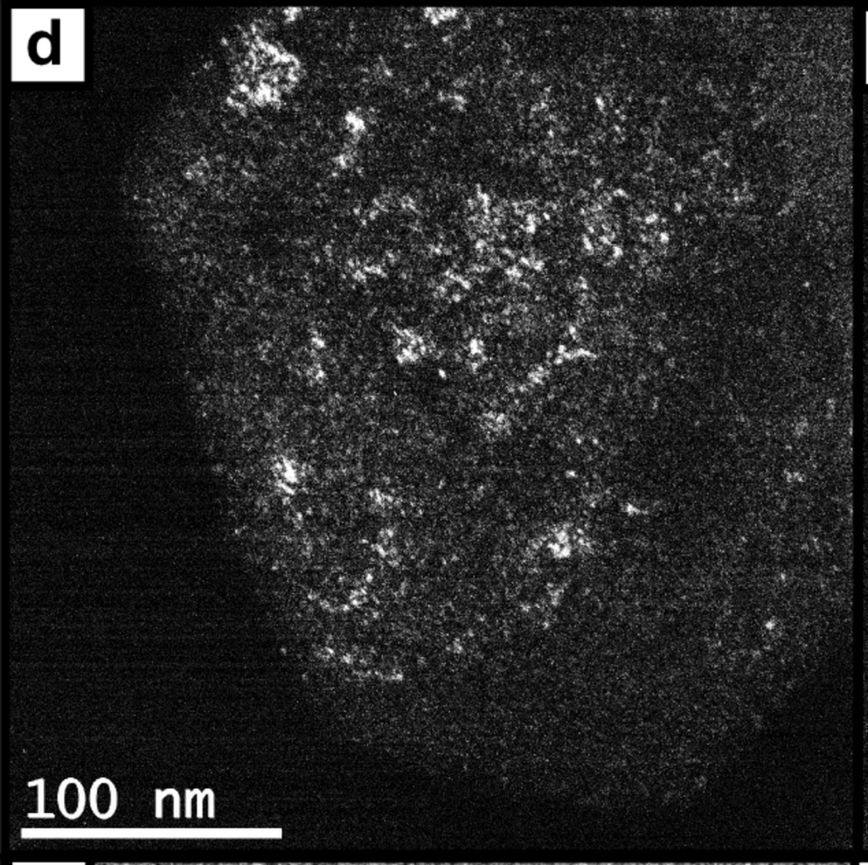
d
100 nm

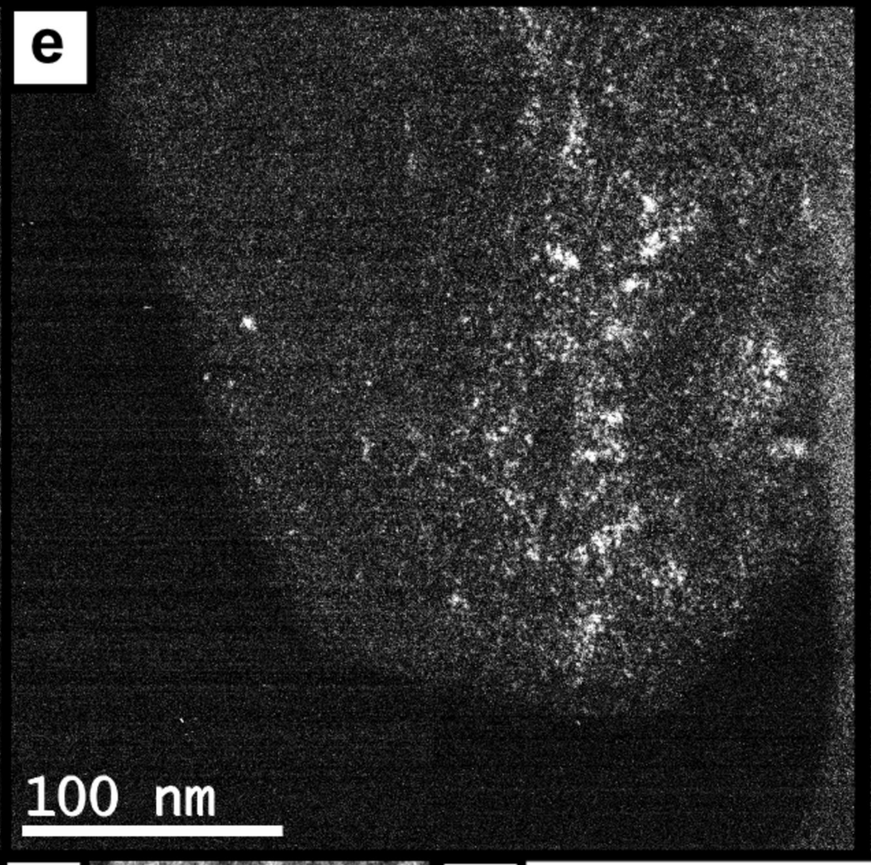
e
100 nm

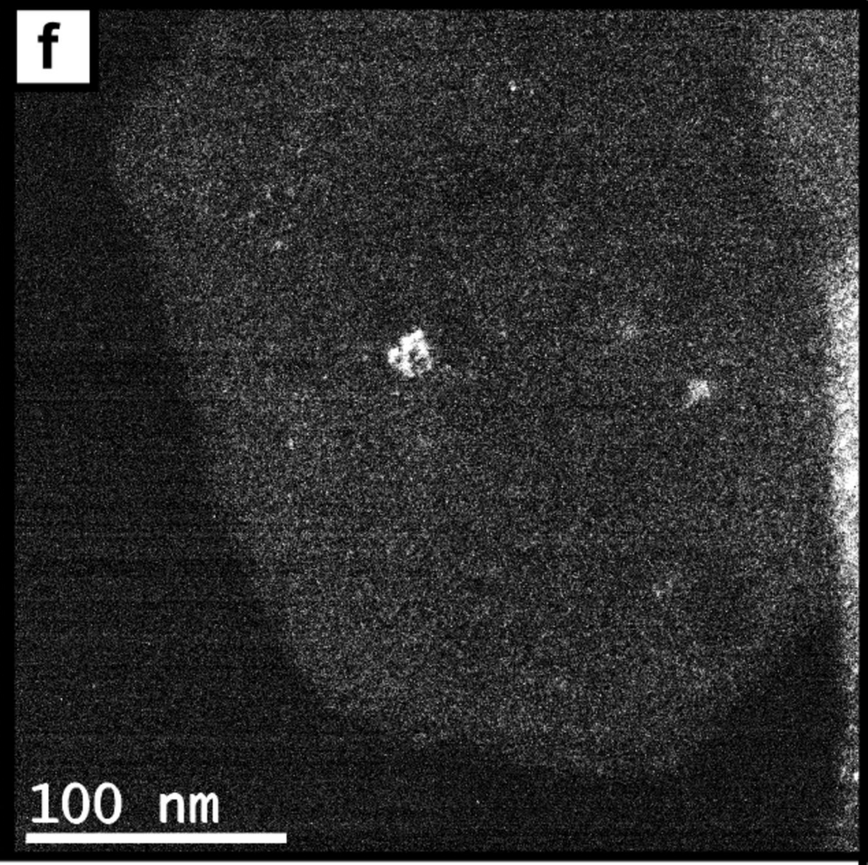
f
100 nm

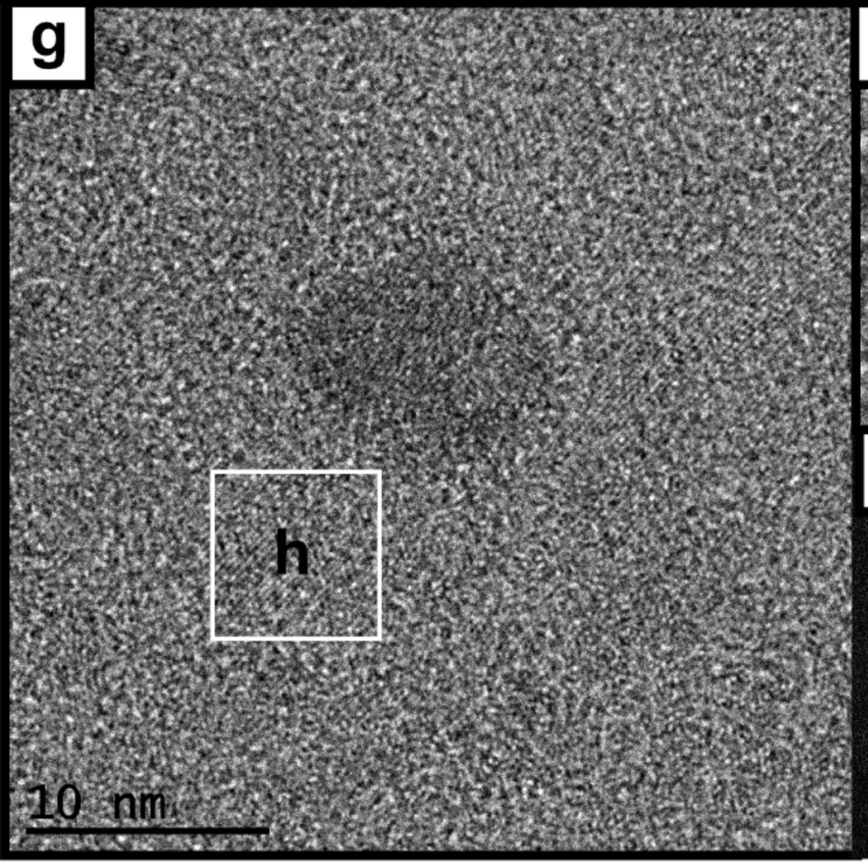
g
h
10 nm

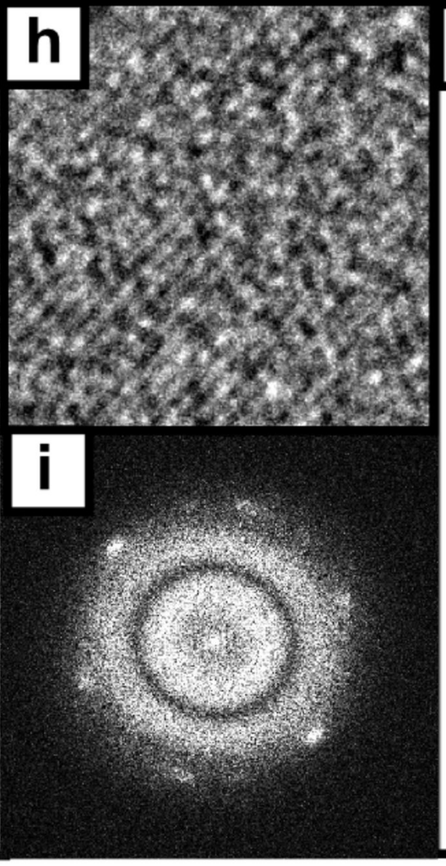
h
i

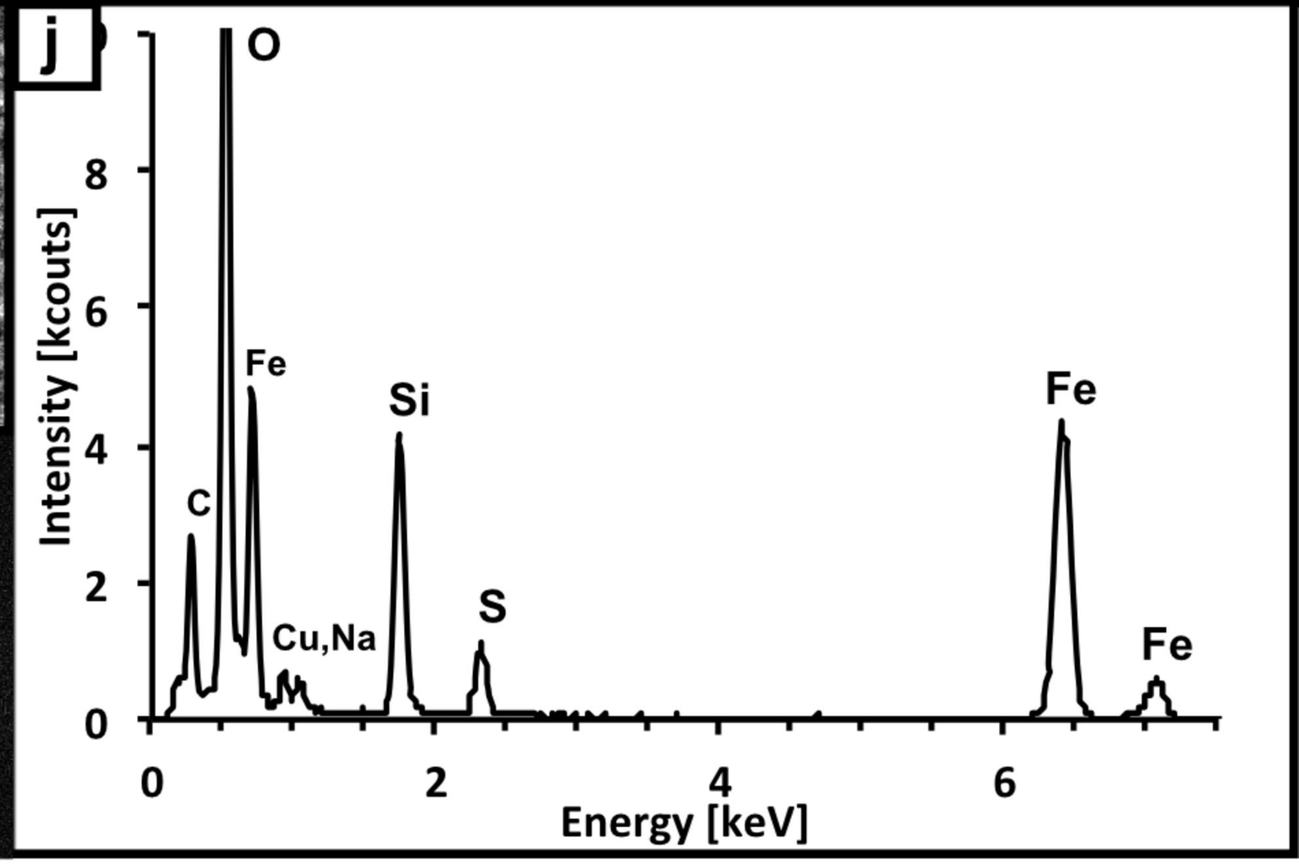
j
O
Fe
Si
C
Cu,Na
S
Fe
Fe
Intensity [kcouts]
0
2
4
6
8
0
2
4
6
Energy [keV]

FIgure 5

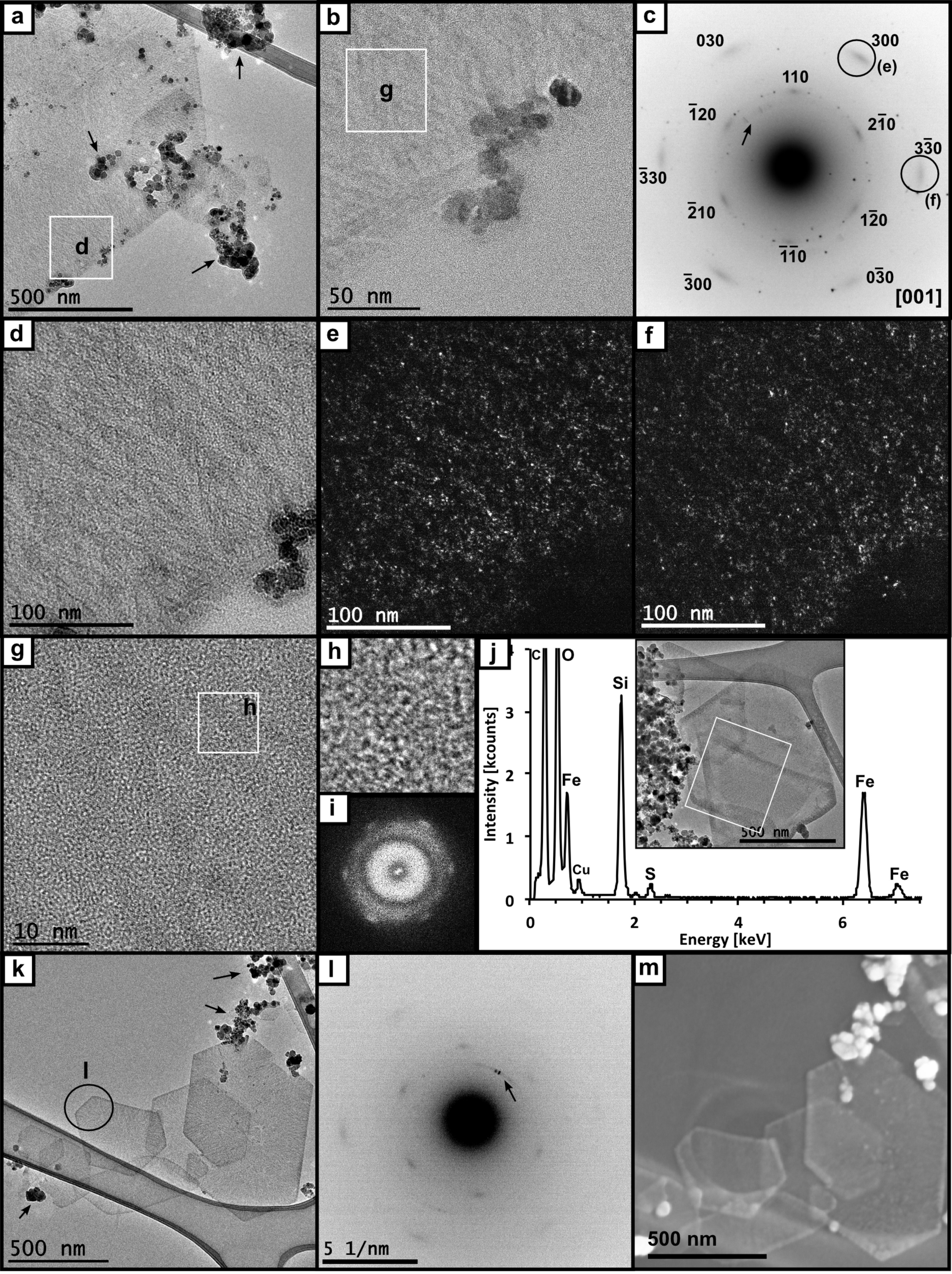
a
500 nm
d
b
g
50 nm
c
030
300
(e)
110
$\bar{1}20$
$2\bar{1}0$
$3\bar{3}0$
$\bar{3}30$
(f)
$\bar{2}10$
$1\bar{2}0$
$\bar{1}\bar{1}0$
$\bar{3}00$
$0\bar{3}0$
[001]
d
100 nm
e
100 nm
f
100 nm
g
h
10 nm
h
i
j
C
O
Si
Fe
Cu
S
Fe
Fe
Intensity [kcounts]
0
1
2
3
0
2
4
6
Energy [keV]
500 nm
k
l
500 nm
l
5 1/nm
m
500 nm

FIgure 6

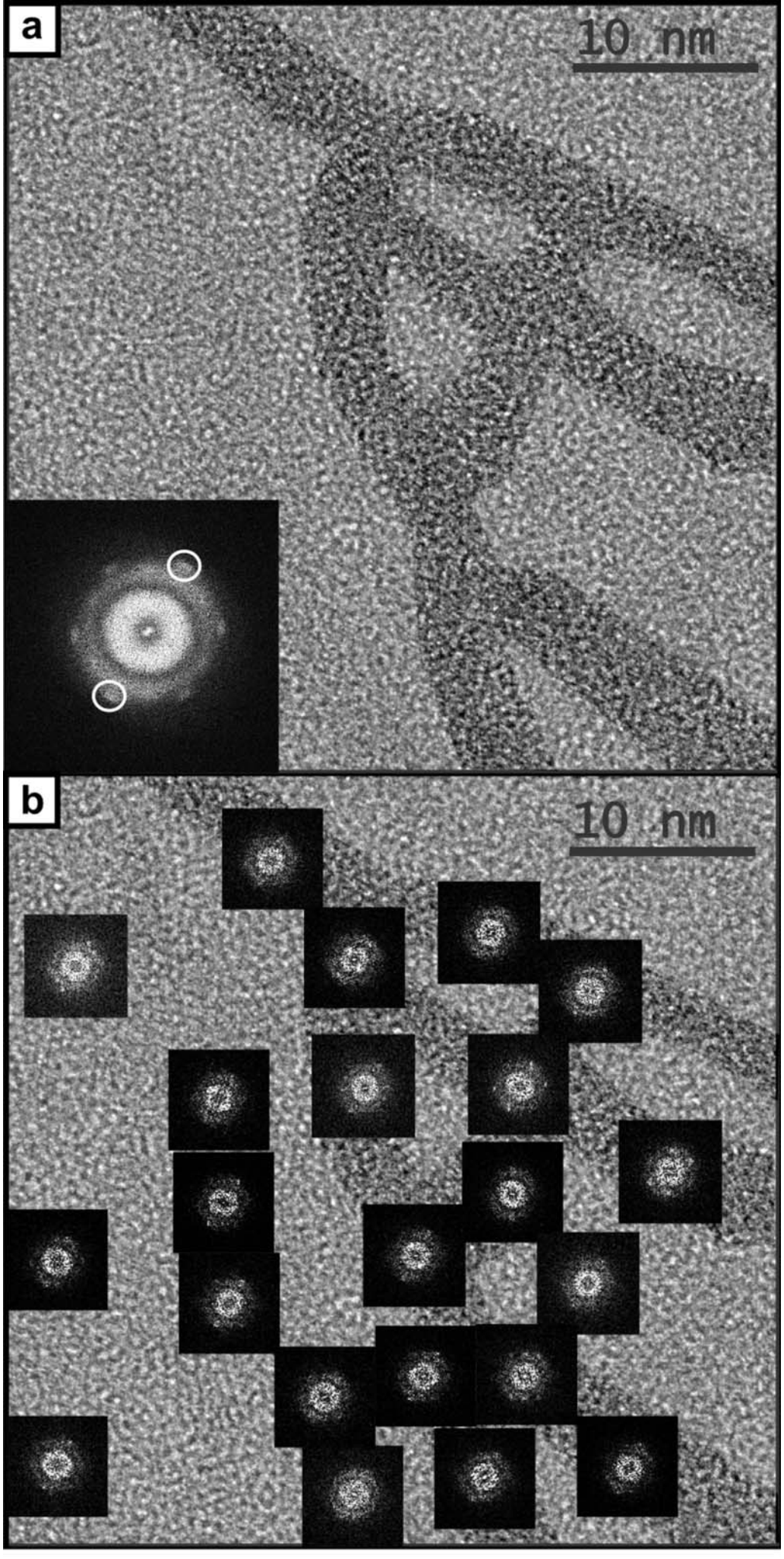

Figure 7

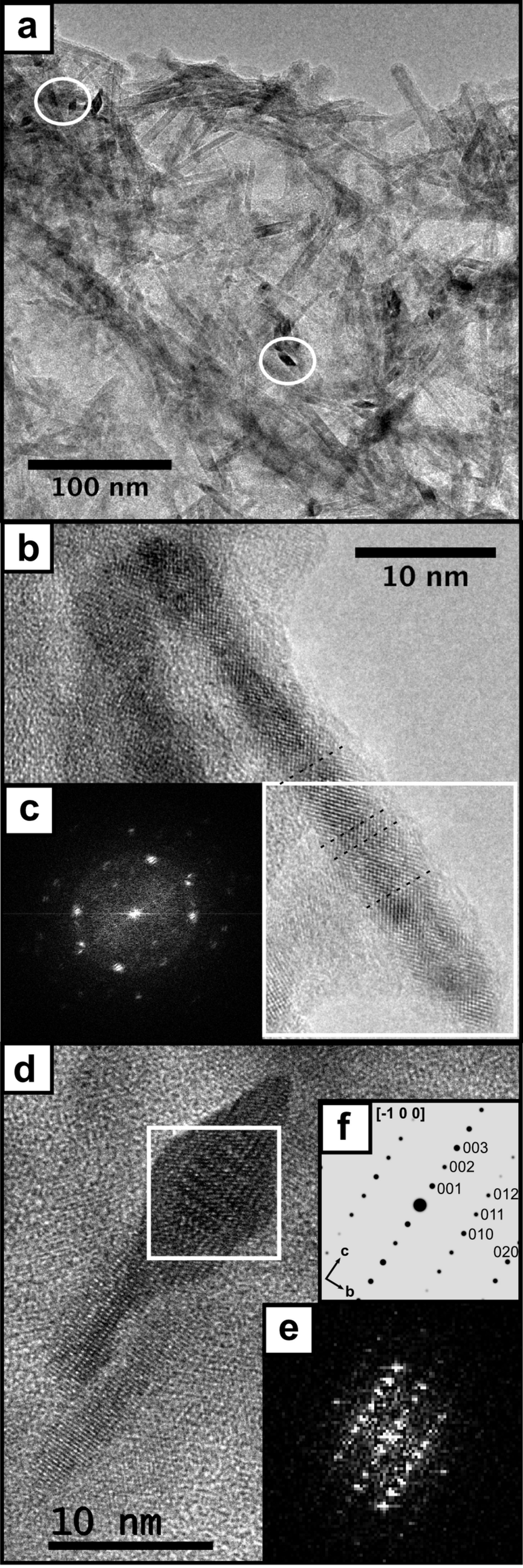

FIgure 8

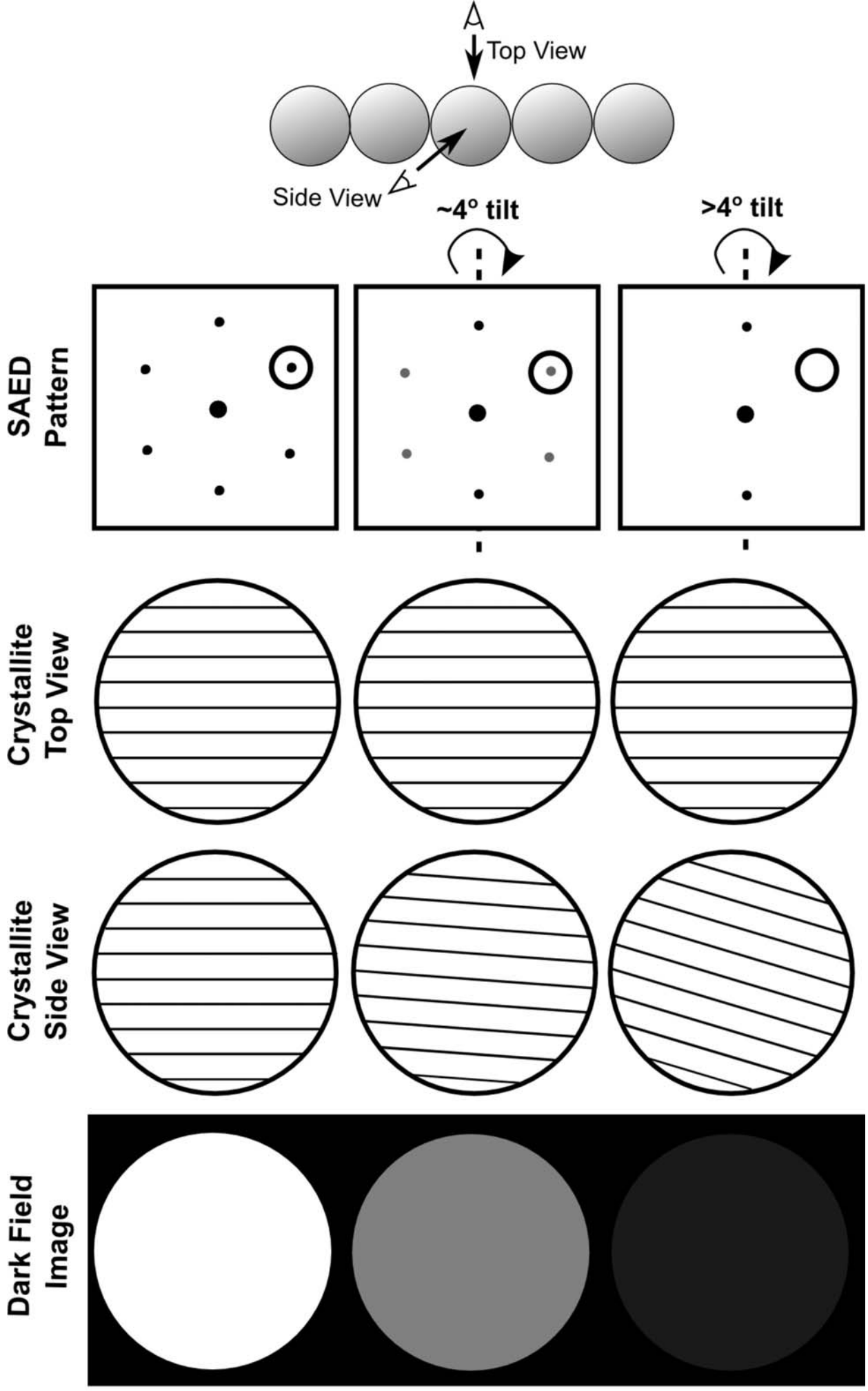
Top View
Side View
~4° tilt
>4° tilt
SAED Pattern
Crystallite Top View
Crystallite Side View
Dark Field Image

Figure 9